12-2021

Theoretical Investigations of the Structural, Dynamical, Electronic, Magnetic, and Thermoelectric Properties of CoRhYSi (Y = Cr, Mn) Quaternary Heusler Alloys

Abdullah Hussain Hzzazi
University of Arkansas, Fayetteville

Citation

Hzzazi, A. H. (2021). Theoretical Investigations of the Structural, Dynamical, Electronic, Magnetic, and Thermoelectric Properties of CoRhYSi (Y = Cr, Mn) Quaternary Heusler Alloys. *Graduate Theses and Dissertations* Retrieved from https://scholarworks.uark.edu/etd/4266

Theoretical Investigations of the Structural, Dynamical, Electronic, Magnetic, and Thermoelectric Properties of CoRhYSi (Y = Cr, Mn) Quaternary Heusler Alloys

A thesis submitted in partial fulfillment
of the requirements for the degree of
Master of Science in Physics

by

Abdullah Hussain Hzzazi
Jazan University
Bachelor of Science in Physics, 2015

December 2021
University of Arkansas

This thesis is approved for recommendation to the Graduate Council.

Bothina H. Manasreh, Ph.D.
Dissertation Director

Hiro Nakamura, Ph.D.
Committee member

Pradeep Kumar, Ph.D.
Committee member

Abstract

Thermoelectric materials have potential properties for utilizing waste heat. The computations are used to estimate the electronic structure of CoRhYSi (Y = Cr, Mn) Quaternary Heusler alloys, as well as their elastic and magnetic characteristics. The full-potential linearized augmented plane wave is used in the calculations. The exchange-correlations are addressed using Perdew–Burke and Ernzerhof's generalized gradient approximation (GGA-PBE). With the exception of CoRhCrSi and CoRhMnSi, which are simple ferromagnets that are approximately half metallic in nature, electronic structure calculations demonstrate that these compounds have a gap in the minority states band and are obviously half-metallic ferromagnets. The magnetic moments of the CoRhCrSi and CoRhMnSi compounds match relatively well with the Slater-Pauling rule, indicating half metallicity and high spin polarization for these compounds. The semi-classical Boltzmann theory was used to compute the Seebeck coefficient (S), electrical conductivity (σ), and electronic thermal conductivity (k_e) of CoRhYSi (Y = Cr, Mn) alloys, whereas Slack's equation was used to get the lattice thermal conductivity (k_L).

Dedication

For their constant support and patience, I dedicate this dissertation to my father, mother, and brothers. Throughout these long years, your prayers have guided me. From the bottom of my heart, I thank you.

This thesis is also dedicated to my father and my mother, who were there for me every night. There are no words to express my thanks for your admirable support and patience. I will always be grateful to both of you, and without you, I am nothing.

Acknowledgments

I would like to express my sincere appreciation to Dr. Bothina H. Manasreh, my thesis chair, for her continuous support and direction throughout my program and this research study. Without her insightful remarks, direction, and support throughout the years, this thesis would not have been possible.

I'd like to express my gratitude to Dr. Hiro Nakamura and Dr. Pradeep Kumar, members of my committee, for their time and valuable suggestion.

I'm also grateful to Hind Alqurashi, a colleague who contributed time, thoughts, critiques, and suggestions to help me finish this thesis.

Table of Contents

List of Tables

List of Figures

Chapter 1: Introduction and Overview

The increasing demands for fossil fuels due the vast leap in technology has urged the search for other alternative sources of energy. In addition, the intensive use of fossil fuels for most of public transport and industrial production created other problems such as pollution and global climate change. Regarding the energy consumption, the waste heat is one of the problems, where 75% of energy consumption is in the form of thermal energy, and the mechanical power utilizes only 25% of the energy[1], [2]. Therefore, scientists have been searching for other alternative resources that have a sustainability and can use this waste of heat. One of these resources is the thermoelectric generators, which are renewable and environmentally friendly source of energy that can transform waste heat to electricity [3].

The thermoelectric devices are composed of p- and n-type of semiconductors that are connected electrically in series and thermally in parallel. On one hand, they can operate as thermal generators of voltage as a result of temperature gradient between the two sides of the thermoelectric modules in a phenomenon known as the Seebeck effect [4] (Figure 1a). On the other hand, they can be used in refrigeration, where the heat transfers from one side to the other side of the module by applying an electric current in a phenomenon known as Peltier effect [5] (Figure 1b). Thermoelectric materials have become one of the most promising resources of energy owing to the low cost of production, the eco-friendly electricity generation, the sustainability, fewer moving parts and less maintenance. Thermoelectric materials have been very successful in transforming waste heat into electricity in several applications such as radioisotope thermoelectric generators in NASA's spacecrafts [6]. The research in this field was focused on application such as geometry, cooling, shape, size, and also the adaptation of the heat flow of systems [7]–[9].

Heusler alloys are promising materials for thermoelectric applications. There are several properties that make Heusler alloys interesting such as half metallicity, ferromagnetistm, spin gapless semiconducting, superconductivity, semiconducting, and shape memory effect [10]–[13].

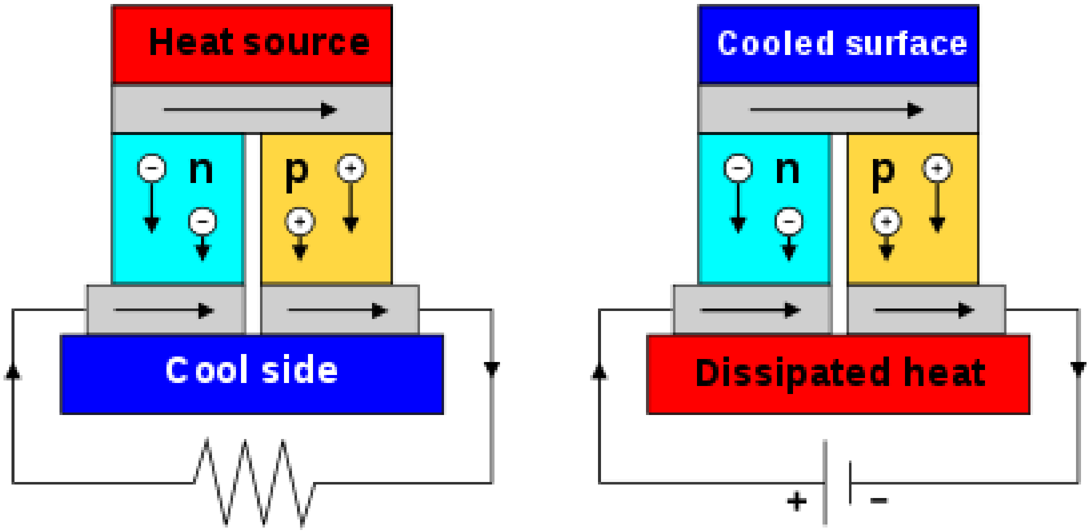

(a) (b)

Figure 1. (a) Seebeck effect thermocouple. (b) Peltier effect thermocouple.

Chapter 2: Background

2.1 Heusler Compounds

Since their discovery, Heusler compounds have attracted a lot of attention [14]. Owing to their interesting features, such as the high Curie temperature and high spin polarization, these compounds have become one of the forefront research topics for applications such as spin injectors and magnetic tunnel junctions[15]–[22]. Furthermore, Heusler compounds have sparked interest due to their potential thermoelectric properties, which might be utilized to generate energy in thermoelectric generators[23]–[28]. There are four types of Heusler alloys, namely, full, inverse, half and quaternary Heusler compounds. The chemical structure of full Heusler compounds is X_2YZ, where X and Y are transition or rare-earth metallic atoms, and Z is the main group element. The valence electrons of a Y transition metal atom are smaller than those of an X transition metal atom. They crystallize in the $L2_1$ structure, which belongs to the $Fm\bar{3}m$ space group with a unit cell of four interpenetrating face-centered cubic sublattices, as seen in Figure 2 [29]. The chemical structure of the inverse full Heusler compounds is X_2YZ, which is the same as the full Heusler compound except that the valence electrons of the X atom are less than the those of Y atom with Hg_2TiCu prototype [30]. Half Heusler compounds, on the other hand, possess the chemical formula of XYZ, with one of the four sublattices unfilled. These alloys have a $C1_b$ crystal structure with an $F\bar{4}3m$ space group [31]. The quaternary Heusler compound X X'YZ is created by substituting one of the X transition metal atoms in the full Heusler compound with another (X'), where Y has less valence electrons than X' and the latter has fewer valence electrons than X. The quaternary Heusler compound structure is Y-type and has an $F\bar{4}3m$ (#216) space group[32]. The Heusler compounds have unique magnetic characteristics due to the partially filled *d* states of the transition metal atoms. When compared to pseudoternary compounds such $Co_2Fe_{1-x}Mn_xZ$, the

$Co_2Fe_{1-x}Mn_xZ$, the quaternary Heusler compounds have lower power dissipation due to lower disorder scattering resistivity [33].

	A	B	C	D
Full Heusler	X	Y	X	Z
Half Heusler	X	Y		Z
Quaternary Heusler	X	Y	X’	Z
Inverse Heusler	X	X	Y	Z

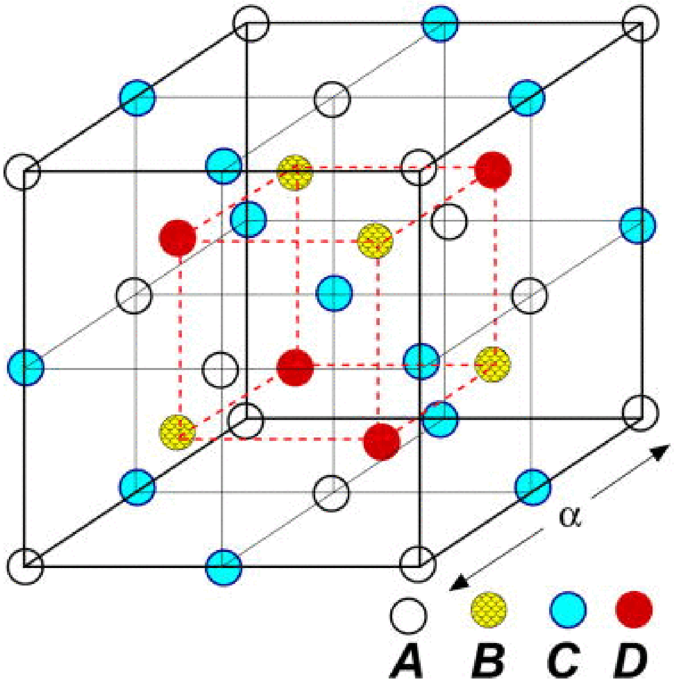

Figure 2. The different structures of the Heusler compounds [33].

A little change in the lattice constant may lead to a transition from half-metallic to metallic behavior of most half-metallic structures[34]–[36]. The electrical and magnetic properties of a compound are determined by the crystal's geometrical structure, with different atomic orders presenting unique electronic and magnetic properties [33]. The density of states schematics for various Heusler compounds are shown in Figure 3. The band structure of some Heusler compounds was discovered to be distinct from that of metals and semiconductors, with one spin channel band structure operating as a metal and the other spin channel operating more like a semiconductor [34], [37]. This is referred to as a half-metallic ferromagnetic behavior (HMF).

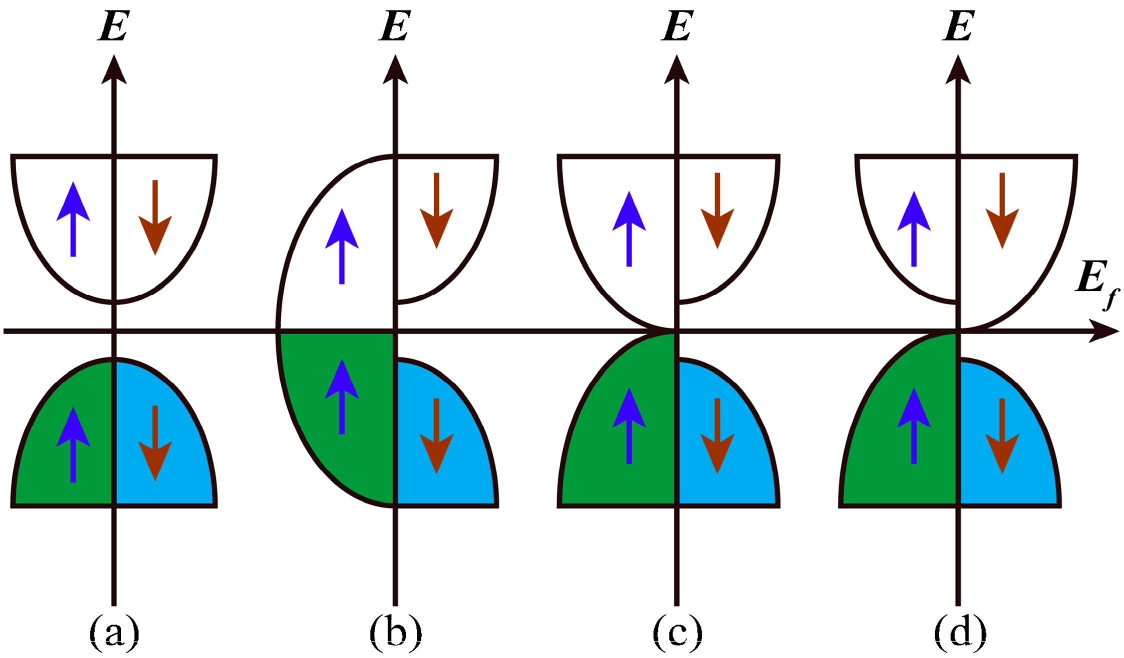

Figure 3. Schematics diagrams of the density of states for (a) metallic, (b) semiconductor, (c) HMF, and (d) spin gapless semiconductor [19].

The high spin polarization of half-metallic ferromagnetism is the result of the half-metallic ferromagnetism. At the Fermi energy, the spin polarization can be used to describe the electronic properties. The spin polarization (P) is calculated as follows [38]:

$$P = \frac{\rho_{up}(E_F) - \rho_{dn}(E_F)}{\rho_{up}(E_F) + \rho_{dn}(E_F)} X\ 100\% \qquad \text{(Equation 1)}$$

where ρ_{up} (E_F) and ρ_{dn} (E_F) are the spin up and spin down density of states at the Fermi level (E_F), respectively. The 100% spin polarization (P =100 %) indicates a complete half-metallicity that corresponds to a zero density of states in either spin up or spin down channel. The relationship between the concentration of valence electrons and the total spin magnetic moment is represented by the Slater-Pauling rule. Heusler compounds are widely known to follow this rule [12], [39], [40], which is used to anticipate the compound's total spin magnetic moment. The Slater-Pauling rule is defined as follows:

$$M_{tot} = (Z_{tot} - 2N_{\downarrow})\mu_B \qquad \text{(Equation 2)}$$

The total magnetic moment is M_{tot}, while the number of total valence electrons and spin-down valence electrons are Z_{tot} and $N_{\downarrow}$, respectively.

The dimensionless figure-of-merit can be used to calculate the thermoelectric efficiency of materials, which is expressed as follows:

$$ZT = S^2\sigma T/(K_L + K_e) \qquad \text{(Equation 3)}$$

where S is the Seebeck coefficient, σ is the electrical conductivity. In addition K_L and K_e are the lattice and electronic thermal conductivities, respectively [41]. A high *ZT* value indicates that the thermoelectric material has a higher conversion efficiency. As shown in Equation, the value of the *ZT* has no limit. By increasing the Seebeck coefficient or electrical conductivity, or decreasing the lattice thermal conductivity, the *ZT* value can be enhanced. Increasing electrical conductivity, on the other hand, increases the electronic thermal conductivity. As a result, the best thermoelectric materials have a *ZT* of less than one (≈ 1). The thermoelectric properties are widely known to be dependent on the electronic structure. According to the following equation, an increase in the effective mass or a decrease in the carrier concentration causes a rise in the material's Seebeck coefficient:

$$S = \frac{8\pi^2 k_B^2 T}{3eh^2} m^* (\frac{\pi}{3n})^{2/3}. \qquad \text{(Equation 4)}$$

In this equation, Boltzmann constant, electronic charge, Planck's constant, effective mass, and carrier concentration are represented as k_B, e, h, m^*, and n, respectively. Furthermore, according to the following relation [42], high mobility (μ) and a small band gap improve electrical conductivity:

$$\sigma = ne\mu \qquad \text{(Equation 5)}$$

High S, and σ values are attributes of the best thermoelectric material, resulting in a high-power factor (PF):

$$PF = S^2\sigma \qquad \text{(Equation 6)}$$

The thermopower (Seebeck coefficient) of a material is an intrinsic feature that can be defined as the ratio of the voltage developed to 1 K temperature difference (ΔV/ΔK). Metals have a very low Seebeck coefficient, with most metals expressing less than 10 μV K^{-1} [43]. Furthermore, at any temperature, the electrical to thermal conductivity ratio remains constant. Therefore, metals have low ZT values. Semiconductors, on the other hand, have larger power factors than metals [44], making them a better choice for thermoelectric materials [44], [45]. The negative (positive) Seebeck coefficient is referred to as n-type (p-type) material. The Seebeck coefficient is calculated using the following formula for different carrier types [46]:

$$S \approx \frac{(S_n\sigma_n + S_p\sigma_p)}{(\sigma_n + \sigma_p)} \qquad \text{Equation 7}$$

where n (p) indicates n-type (p-type) materials, which the electrons or holes function as charge carriers. Due to the complicated scattering mechanism involving defect, phonon, and carrier scattering, estimating the charge carrier scattering relaxation time in the Boltzmann equation is challenging. As a result, constant relaxation time approximation is a good approach that has been utilized to evaluate the transport properties of most materials [47]. The merit figure can be written as:

$$ZT = (S^2\sigma T/k_e)\ X\ (k_e/k_L + k_e)) \qquad \text{Equation 8}$$

where ZT = (S^2T/K_e) defines the upper limit of the ZT value and is independent of the relaxation time. At high temperatures, K_e surpasses K_L, resulting in (k_e/(k_L+ k_e) ≈ 1, allowing ZT_e to be an excellent approximation to the ZT value at high temperatures [48]. At low temperatures, the value of k_e is low, and the k_L value take priority.

Due to their high Curie temperatures and low band gaps, Heusler compounds have become a strong competitor as thermoelectric materials. They have a high Seebeck coefficient and electrical conductivity, which leads to a high thermoelectric power factor [16], [28], [49], [50]. Some Heusler compounds have ZT values that are comparable to cutting-edge thermoelectric materials [28], [51].

2.2 Literature review

The electronic and magnetic electronic transport properties were intensely investigated for full- and half-Heusler compounds. The full-Heusler compounds were the most investigated of the various forms of Heusler compounds. Due to their half-metallic nature and high Curie temperatures, cobalt-based full-Heusler compounds have attracted a lot of interest [52]. Heusler compounds have recently attacked a lot of interest. Some of these compounds have shown promising properties as spintronic devices and thermoelectric materials [12], [53]–[55]. Compounds such as CoFeMnSi, CoFeCrAl, CoMnCrSi, CoFeVSi, and FeMnCrSb have shown a spin gapless semiconducting behavior [56]. Furthermore, ab initio electronic structure computations for CoFeMnZ (Z = Al, Ga, Si, or Ge) compounds with high Curie temperatures revealed a half-metallic ferromagnetic structure [33]. For CoTcMnSi and CoRhMnSi compounds, Kundu et al. predicted high Curie temperatures and half-metallic behavior [49]. Heusler compounds have also been thoroughly researched for their potential as good thermoelectric materials for energy harvesting and refrigeration [26], [48], [57]. The thermoelectric efficiency of several materials is depicted in the diagram.

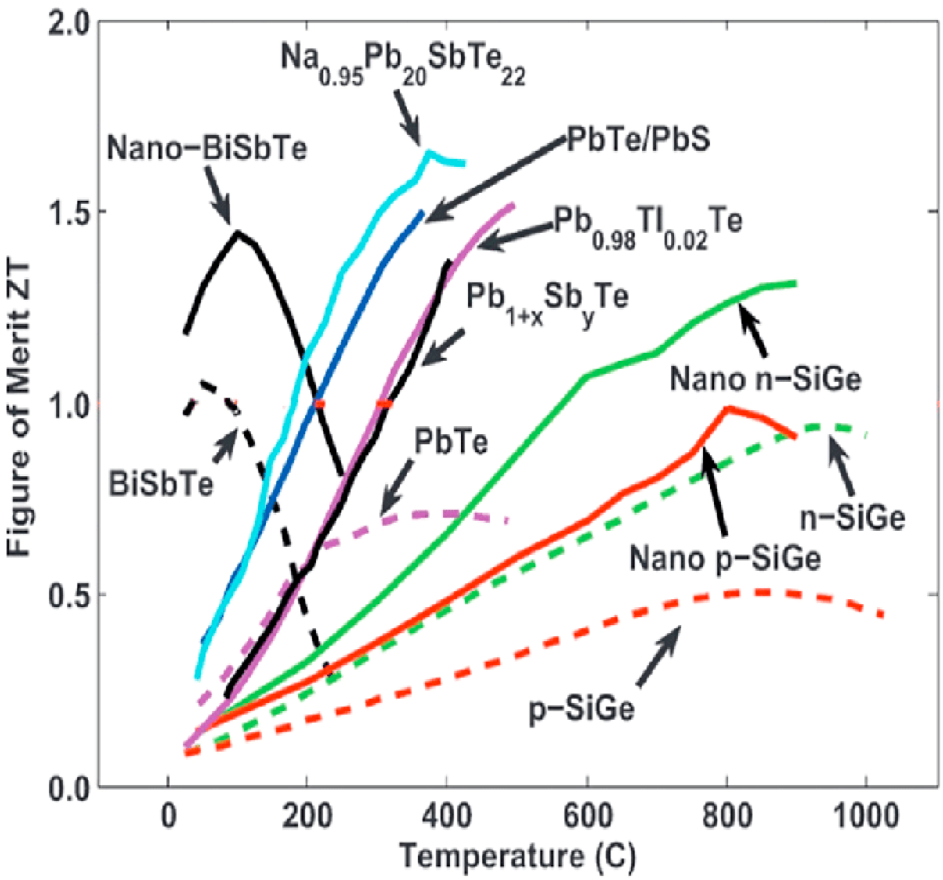

Figure 4. The figure of merit versus temperature of thermoelectric materials [51].

The Curie temperature and the concentration of valence electrons are linearly related in cobalt-based Heusler compounds [38]. For substances with a significant number of valence electrons, the Curie temperature is observed to be the highest. Experimentally, Co_2FeSi has the greatest Curie temperature of 1100 K among other alloys with a total spin magnetic moment of 6 μB [58]. These findings matched those of theoretical research using ab initio calculations [59], [60].

Chapter 3: Method of Calculation

3.1 Quantum Theory

In this chapter, the relation between the quantum theory and Boltzman transport theory are explained. Without the quantum theory, it is impossible to investigate the electrons behavior in the materials. Transmuting heat and electricity are the responsibility of the electrons in the materials.

3.1.1 Schrödinger Equation

The many-body problem is explained by the time dependent Schrödinger equation that is given by the following form:

$$i\hbar \frac{\partial \Phi(\mathrm{r,t})}{\partial t} = -\frac{\hbar^2}{2m}\nabla^2\Phi(\mathrm{r,t}) + V\Phi(\mathrm{r,t}) \qquad \text{Equation 9}$$

$$\frac{\hbar^2}{2m}\nabla^2\Phi(\mathrm{r,t}) + V\Phi(\mathrm{r\ t}) = E\Phi(\mathrm{r}) \qquad \text{Equation 10}$$

Here $\hbar$ is referred to the reduced Plank constant, $\Phi(\mathrm{r,t})$ is the wavefunction of the ions and electrons, m is the reduced mass, V is the potential, r is nuclei and electron coordinates. E is replaced by $i\hbar\frac{\partial}{\partial t}$ and is considered independent of time. The ∇^2 is $\frac{\partial^2}{\partial x^2}$, the $\frac{\hbar^2}{2m}$ and $\frac{\partial^2}{\partial x^2}$ is called the Hamiltonian, which is the total energy of the system. The energy was independent of time in this project.

The Hamiltonian form is:

$$H = \hat{T} + \hat{V} \qquad \text{Equation 11}$$

which is the sum of the kinetic and potential energies. The kinetic energy is defined as:

$$T = \frac{p^2}{2m} \qquad \text{Equation 12}$$

where the momentum is an operator define as $P = -i\hbar\,\frac{\partial}{\partial x}$. Therefore, the Schrödinger Equation takes a form as:

$H\Phi = E\Phi$ Equation 13

These previous equations are for a single particle. Thus, searching for the most stable state of many-body problem should be established, which is the ground state of the system. The many-body problem Schrödinger Equation should be solved to find the ground state of many-body system. Therefore, the time independent Schrödinger Equation can be given by:

$H\Phi(r_i, R_i) = E\Phi(r_i, R_i)$ Equation 14

The many-body Schrödinger Equation of a system that contains of N nuclei with the coordinates of $R_i \ and \ N_e$ and electrons with coordinates of r_i. The interaction between nuclei-electrons, nuclei-nuclei, and electron-electron should be studded in many-body problems. By utilizing all these interactions and adding to the kinetic energies of electrons and nuclei, the Hamiltonian can be given as:

$H = T_N(R) + T_e(r) + V_{NN}(R) + V_{Ne}(R, r) + V_{ee}(r)$ Equation 15

The H is the Hamiltonian operator, which is the sum of kinetic energy of the nuclei T_N and an electron T_e and the potential energy of nucleus-nucleus (V_{NN}), electron-nucleus (V_{Ne}), and electron-electron (V_{ee}) interaction. These terms can be extracted as follows:

$T_N = \frac{\hbar^2}{2m_N} \sum_{N=1}^{N} \nabla_N^2$ Equation 16

Where T_N is the kinetic energy of the nuclei, N is the index shows the number of nuclei and m_N is the effective mass of the nuclei.

$T_e = -\frac{\hbar^2}{2m_e} \sum_{i=1}^{N} \nabla_i^2$ Equation 17

Where T_e is the kinetic energy of the electrons, i shows the number of the electrons, and m_e is the effective mass of the electron.

$V_{NN} = \sum_{i>J} \frac{Z_I Z_e e^2}{|R_I - R_J|}$ Equation 18

Where V_{NN} is the coulomb interaction between nuclei, $Z_I \; and \; Z_e$ are the atomic number of each nuclei, e^2 is the charge, and $R_I - R_J$ is the distance between them.

$$V_{eN} = -\sum_{i,I} \frac{Z_I e^2}{|R_I - r_j|} \qquad \text{Equation 19}$$

Where V_{eN} is the interaction between the nuclei and the electrons, $R_I - r_j$ are the distance between electron and nucleus.

$$V_{ee} = \sum_{i>j} \frac{e^2}{|r_i - r_j|} \qquad \text{Equation 20}$$

Where V_{ee} is the electron and electron interaction, $r_i - r_j$ are the distance between the electron-electron.

For many body problems, the equation 15 is a complex equation has several terms and cannot be solved except for a simple issue such as the hydrogen atom. Therefore, it is important to apply some approximation in this equation to solve it.

3.1.2 Born-Oppenheimer Approximation

Due to the mass of electron is less than the mass of proton by four orders of magnitude, the Born-Oppenheimer approximation is supposed that the position of the nuclei is fixed. Thus, if the position of the nuclei is fixed, the terms $T_N(R)$ and $V_{NN}(R)$ are neglected. Then, the Hamiltonian can be:

$$H_e = T_e(r) + V_{Ne}(R, r) + V_{ee}(r) \qquad \text{Equation 21}$$

$$H_e = T_e = -\frac{\hbar^2}{2m_e} \sum_{i=1}^{N} \nabla_i^2 + V_{eN} = -\sum_{i,I} \frac{Z_I e^2}{|R_I - r_j|} + V_{ee} = \sum_{i>j} \frac{e^2}{|r_i - r_j|} \qquad \text{Equation 22}$$

Where H_e is the Hamiltonian of the electrons. Thus, the Schrödinger Equation can be written as:

$$\{T_e(r) + V_{Ne}(R, r) + V_{ee}(r)\}\psi_n^N = E\psi_n^N \qquad \text{Equation 23}$$

For many-body problem, this equation is still complicated to solve the system due to the large number of electrons. So, there are more approximations should be considered to solve this equation.

3.1.3 Hartree and Hartree-Fock Approximations

Transforming the many-body problem to a one body problem was created by Hartree, who solve the Schrödinger equation by taking the one electron wavefunction as a product of the wavefunction of the system [61]. Therefore, the wavefunction of the many-body problem is:

$$\psi(\overrightarrow{r_1}, \dots, \overrightarrow{r_N}, S_1, \dots, S_N) \qquad \text{Equation 24}$$

where $\overrightarrow{r_1}$ is the position of the electron and S is the spin of electron. For two body problem, the total wavefunction is written as:

$$\psi(\overrightarrow{x_1}, \overrightarrow{x_2}) = \psi_1(\overrightarrow{x_1}) |\, S_1\rangle \psi_2(\overrightarrow{x_2}) |\, S_2\rangle \qquad \text{Equation 25}$$

This equation does not content the Pauli exclusion principle of the electrons because it is a symmetric wavefunction which means there are no two electrons have similar quantum numbers. The fermions have half-integral intrinsic spin. This led to Hartree-Fock approximation that solved this issue by combining the wavefunction of Hartree product:

$$\psi(\overrightarrow{x_1}, \overrightarrow{x_2}) = \frac{1}{\sqrt{2}} \{\psi_1(\overrightarrow{x_1}) |\, S_1\rangle\, \psi_2(\overrightarrow{x_2}) |\, S_2\rangle - \{\psi_1(\overrightarrow{x_2}) |\, S_2\rangle \psi_2(\overrightarrow{x_1}) |\, S_1\rangle$$

$$= \frac{1}{\sqrt{2}} \begin{vmatrix} \psi_1(\overrightarrow{x_1}) |\, S_1\rangle & \psi_2(\overrightarrow{x_1}) |\, S_1\rangle \\ \psi_1(\overrightarrow{x_2}) |\, S_2\rangle & \psi_2(\overrightarrow{x_2}) |\, S_2\rangle \end{vmatrix} \qquad \text{Equation 26}$$

By extending the two-body system to many-body system:

$$\psi(\overrightarrow{x_1}, \overrightarrow{x_2}) = \frac{1}{\sqrt{N!}} \begin{bmatrix} \psi_1(\overrightarrow{x_1}) |\, S_1\rangle & \psi_1(\overrightarrow{x_2}) |\, S_2\rangle & \dots & \psi_1(\overrightarrow{x_N}) |\, S_N\rangle \\ \psi_1(\overrightarrow{x_2}) |\, S_2\rangle & \psi_2(\overrightarrow{x_2}) |\, S_2\rangle & \dots & \psi_2(\overrightarrow{x_2}) |\, S_2\rangle \\ \vdots & \vdots & & \vdots \\ \psi_N(\overrightarrow{x_2}) |\, S_2\rangle & \psi_N(\overrightarrow{x_2}) |\, S_2\rangle & \dots & \psi_N(\overrightarrow{x_N}) |\, S_N\rangle \end{bmatrix} \qquad \text{Equation 27}$$

By solving the next Schrödinger equation, each of wavefunction can be pulled out:

$$\left(-\frac{\hbar^2}{2m}\nabla_i^2 + V\right) = E_i\psi_i\ (\vec{r}) \qquad \text{Equation 28}$$

3.1.4 Density Functional Theory

In many body problems, one of the great methods to calculate the ground state properties is the Density Functional Theory [62]. Reducing the many body problem to a single body problem was introduced by Thomas and Fermi [63], who wrote the one electron density $\rho(\vec{r})$ as [63]:

$$E_{tot}\,[\rho(\vec{r})] = \frac{\mathbf{3(3\boldsymbol{\pi}^2)^{2/3}}}{\mathbf{10}} \int \boldsymbol{\rho}(\vec{\boldsymbol{r}})^{\frac{5}{3}} \boldsymbol{d}^{\mathbf{3}}\vec{\boldsymbol{r}} - \boldsymbol{Z} \int \frac{\rho(\vec{r})}{\boldsymbol{r}}\, \boldsymbol{d}^{\mathbf{3}}\vec{\boldsymbol{r}} + \frac{\mathbf{1}}{\mathbf{2}} \iint \frac{\boldsymbol{\rho}(\overrightarrow{\boldsymbol{r}_1})\boldsymbol{\rho}(\overrightarrow{\boldsymbol{r}_2})}{|\boldsymbol{r}_1 - \boldsymbol{r}_2|}\, \boldsymbol{d}^{\mathbf{3}}\overrightarrow{\boldsymbol{r}_1}\boldsymbol{d}^{\mathbf{3}}\overrightarrow{\boldsymbol{r}_2} \qquad \text{(Equation 29)}$$

where E_{tot} is the total energy of the system. The electron density is normalized to the total number of electron (N):

$$\int \rho(\vec{r})\, d^3\vec{\boldsymbol{r}} = N \qquad \text{Equation 30}$$

Then, Hohenberg and Kohn derived the basics of the density functional theory, where they proved the ground state properties of a many-body problem are identified by its electronic density. At the density of the system in the ground state, the energy functional achieve lower level [64]. The properties of the system such as wavefunction and the energy can be obtained by the density. Rather than dealing with the wavefunction of 3N variables, solving the electron density that involve the three spatial variables will decrease the dimensionality. As claimed by Hohenberg and Kohn, the total energy functional is:

$$\boldsymbol{E_{tot}}\,[\boldsymbol{\rho}(\vec{\boldsymbol{r}})] = F_{HK}[\boldsymbol{\rho}(\vec{\boldsymbol{r}})] + \int \boldsymbol{\rho}(\vec{\boldsymbol{r}})\, \boldsymbol{V_{eN}}(\vec{\boldsymbol{r}})\, \boldsymbol{d}\vec{\boldsymbol{r}} \qquad \text{Equation 31}$$

Where F_{HK} is the Hohenberg and Kohn functional.

$$\boldsymbol{F}_{HK}\,[\boldsymbol{\rho}(\vec{\boldsymbol{r}})] = T[\rho(\vec{r})] + V[\rho(\vec{r})] = T_0[\boldsymbol{\rho}(\vec{\boldsymbol{r}})] + V_H[\boldsymbol{\rho}(\vec{\boldsymbol{r}})] + V_{xc}[\boldsymbol{\rho}(\vec{\boldsymbol{r}})] \qquad \text{Equation 32}$$

F_{HK} is the sum of the exact kinetic $T[\rho(\vec{r})]$ and electron-electron potential $V[\rho(\vec{r})]$ energy. The T_0 is the kinetic energy of non-interacting particles, V_H is the Hartree potential energy, and V_{xc} is the exchange correlation energy which is the sum of the V_x the exchange and

V_c the correlation potentials. In the Hartree-Fock, the exchange potential is involved, but in the Hartree solution, the exchange potential is not included:

$$V_x = E_{HF} - E_H \qquad \text{Equation 33}$$

The correlation potential is included in the exact total energy, but it is not found in the total energy of Hartree-Fock solution.

$$V_c = E_{exact} - E_{HF} \qquad \text{Equation 34}$$

Then, the total energy function can be written as:

$$\boldsymbol{E}_{tot}\, [\boldsymbol{n}(\vec{\boldsymbol{r}})] = T_0[\boldsymbol{n}(\vec{\boldsymbol{r}})] + V_H[\boldsymbol{n}(\vec{\boldsymbol{r}})] + V_{xc}[\boldsymbol{n}(\vec{\boldsymbol{r}})] + V_{eN}[\boldsymbol{n}(\vec{\boldsymbol{r}})] \qquad \text{Equation 35}$$

The exchange correlation energy functional form is unspecified, so it cannot be calculated. Accordingly, the electron density can be described as a set of wavefunctions which each wavefunction is standing for a single electron, and that is what Kohn and Sham suggested [65]. Hence, the sum of occupied state of Kohn-Sham orbitals (ψ_i) is the ground electron density:

$$n(\vec{r}) = \sum_{i=1}^{occu} \psi_i^*(\vec{r})\, \psi_i(\vec{r}) \qquad \text{Equation 36}$$

Therefore, this equation is considered a solution for a single electron ground state wavefunctions.

$$\left(T + V_{eff}\right)\psi_i = E_i\psi_i \qquad \text{Equation 37}$$

$$V_{eff} = V_{eN} + V_H + V_{xc} \qquad \text{Equation 38}$$

$$V_{eN} = -\frac{1}{4\pi\varepsilon_0} \sum_{n=1} \frac{Z_n e^2}{|\vec{r_i} - \vec{R_n}|} \qquad \text{Equation 39}$$

$$V_H = \frac{1}{4\pi\varepsilon_0} \int \frac{n(\vec{r_j})e^2}{|\vec{r_i} - \vec{r_j}|}\, d\vec{r_j} \qquad \text{Equation 40}$$

$$V_H = \frac{\delta V_{xc}[n(\vec{r})]}{\delta n(\vec{r})} \qquad \text{Equation 41}$$

Thus, the total ground state energy can be:

$$E_{tot}(R_1, \dots, R_n) = \sum E_i - \frac{1}{2} E_H[n_0(\vec{r})] + E_{xc}[n_0(\vec{r})] - \int V_{xc}\rho_0 d\vec{r} + V_{NN}(R_1, \dots, R_n) \qquad \text{Equation 42}$$

The claim that Kohn and Sham introduced makes the density functional theory a partial method, and that help to analyze the ground state density.

3.1.5 Exchange Correlation Energy Approximation

To get the precise of the ground state energy, there are many approximations to evaluate the exchange-correlation energy, and that is calculated by density functional theory. The local density approximation (LDA) and the generalized gradient approximation (GGA) are the universal that used to estimate the exchange-correlation [65], [66].

3.1.6 Local Density Approximation (LDA)

In this approximation, the homogeneous electron gas is an advance exchange-correlation functionals that explains the physics of the LDA exchange and correlation, and the electron density of the system is written as follows:

$E_{xc} = \int n(r)\, \varepsilon_{xc}\big(n(r)\big)dr,$ Equation 43

where $n(r)$ is the electron density, $\big(n(r)\big)$ is the charge density, and it is adequately low. ε_{xc} is the exchange and correlation energy. $\varepsilon_{xc}\big(n(r)\big)$ is an unknown term in this equation [67]. Therefore, $\varepsilon_{xc}\big(n(\vec{r})\big)$ is separated to two contributions which is exchange and correlation terms:

$\varepsilon_{xc}\big(n(\vec{r})\big) = \epsilon_x\big(n(\vec{r})\big) + \epsilon_c\big(n(\vec{r})\big)$ Equation 44

Where ϵ_x is the exchange term where can be solved, and it corresponds to the exchange of an electron in a uniform electron gas [68].

$\varepsilon_x\big(n(r)\big) = -\frac{3}{4}(\frac{3n(r)}{\pi})^{1/3}$ Equation 45

Nevertheless, ϵ_c is the correlation term where can be obtained by using Monte-Carlo simulations [69]. The LDA approximation is only beneficial for a slow varying density. The electron density of a practical system is not uniform.

3.1.7 Generalized Gradient Approximation (GGA)

To achieve more precise approximation, the gradient of the electron density is put into consideration, where the density is changing from one point to another point. By this presumption, the gradient of electron density can be as follow:

$$E_{xc}^{GGA} = \int n(r)\varepsilon_{xc}\big(n(r)\big)\, F(|\nabla \mathrm{n(r)}|)dr \qquad \text{Equation 46}$$

For solids, the generalized gradient approximation (GGA) is performing will. Thus, there are methods to estimate the GGA, which is Perdew-Burke-Ernzerhof (PBE) and PBE-sol [66], [70].

3.1.8 Self-consistent Solution

The electron density can be acquired by calculating the single-particle wavefunction using Koh4n-Sham equations, where the wavefunction can be attained. Hence, the self-constant interaction is neglected [71]. The exchange-correlation energy is written as follows:

$$E_{xc} = E_x^{exact} + E_c \qquad \text{Equation 47}$$

Only for one-center system, this approximation offers an acceptable result, but it is irrelevant to description of chemical bond in molecules [72], [73]. This situation is explained by the Coulomb correlation energy, dynamic correlation (short-range), and nondynamic correlation (long-range) [74]. For short distance, since the electrons with opposition spin reach one another, the dynamic element is customized as the Coulomb correlation [A]. E_x^{DFT} is the semi-local exchange functionals, which written as DFT = LDA, GGA that takes the nondynamic correlation into the account and is written as compact form [75].

$$E_{xc} = E_x^{DFT} + E_c^{DFT} = (E_x^{exact} + E_c^{nd}) + E_x^{DFT} \qquad \text{Equation 48}$$

The self-consistent interaction and nondynamic correlation is accounted in a balanced way. The final form of hybrid exchange correlation functional was introduced by Becke which is a linear combination of these functionals depend on the adiabatic binding formalism of Khon-Sham's fictitious system [76].

$$E_{xc}^{hybr} = a_0 E_x^{exact} + (1 - a_0) E_x^{LDA} + a_x \Delta E_x^{B88} + E_c^{LDA} + a_0 \Delta E_c^{GGA}$$

$$a_0 = 0.2, \qquad a_x = 0.72, \qquad a_c = 0.81.$$

By putting the theoretical result, a_0, a_x, and a_c can be found with the experimental results. From the exchange correlation that is taken from the B88, the ΔE_x^{B88} can be obtained as a correction to gradient exchange, and ΔE_c^{GGA} is a correction to gradient correlation [77].

3.1.8 Boltzmann Transport Theory

The Boltzmann transport equation describes the relaxation heat conduction which, and how the electron administrates the relation between the heat flux, thermal gradient, and fractional Fourier law [78]. The generalizing the collision term is the main goal of this study [78]. At equilibrium, Fermi-Dirac distribution function $f_0(\varepsilon)$:

$$f_0 = \frac{1}{1+EXP(\frac{\varepsilon(k)-\mu(r)}{k_B T(r)}} \qquad \text{Equation 49}$$

Where ε is the electric energy, μ is the chemical potential, k_B is the Boltzmann constant, and T is the absolute temperature. The external perturbation does not exist, so there is not change in the distribution function. On the other hand, the position and momentum of electrons are changing under external perturbation of the thermal gradient. Relaxation time approximation is a method that adapted to have a precise solution of the Boltzmann transport equation because it is complicated.

$$\frac{\partial f}{\partial t} = -\frac{f - f_0}{\tau} \qquad \text{Equation 50}$$

After the external perturbation disappeared, the perturbed distribution function f will restore to its equilibrium distribution.

$$\sigma_{\alpha\beta}(T,\mu) = \frac{1}{\Omega}\int \sigma_{\alpha\beta}(\varepsilon)\left[-\frac{\partial f_{\mu}(T,\epsilon)}{\partial\varepsilon}\right] d\varepsilon$$

Equation 51

$$k_{\alpha\beta}(T,\mu) = \frac{1}{e^{2}T\Omega}\int \sigma_{\alpha\beta}(\varepsilon)(\varepsilon-\mu)^{2}\left[-\frac{\partial f_{\mu}(T,\epsilon)}{\partial\varepsilon}\right] d\varepsilon$$

Equation 52

$$S_{\alpha\beta}(T,\mu) = \frac{1}{eT\Omega\sigma_{\alpha\beta}(T,\mu)}\int \sigma_{\alpha\beta}(\varepsilon)(\varepsilon-\mu)\left[-\frac{\partial f_{\mu}(T,\epsilon)}{\partial\varepsilon}\right] d\varepsilon$$

Equation 53

$$\sigma_{\alpha\beta} = \frac{e^{2}}{N_{k}}\sum\nolimits_{i,k} \tau\, v_{\alpha}(i,k) v_{\beta}(i,k)\frac{\delta(\varepsilon-\varepsilon_{i,k})}{d\varepsilon}$$

Equation 54

Where σ is the electrical conductivity, k_e is the electric thermal conductivity, S is the Seebeck coefficient, α and β are tensor components, and $\Omega, v, and\ N_k$ are the chemical potential.

Chapter 4: CoRhYSi (Y= Mn, Cr) Quaternary Heusler Compounds

4.1 Introduction

Quaternary Heusler alloys are a class of Heusler compounds that consist of four different atoms in the unit cell with a space group of F43m (#216). The chemical formula is XX_0YZ, where X, X_0, and Y are transition metal atoms and Z is a metalloid atom. When the number of valence electrons of the X atom is larger than those of X_0 and Y atoms and the number of valence electrons of Y atom is less than that of X_0, the structure is mostly stable [53]. Quaternary Heusler compounds have a Y-type crystal structure with three different atomic configurations as shown in Table 1 and Figure 5 [53].

Table 1. The three different types of crystal structure of the quaternary Heusler compounds.

Type	**4a**	**4c**	**4b**	**4d**
	(0,0,0)	(1/4,1/4,1/4)	(1/2,1/2,1/2)	(3/4,3/4,3/4)
Y-type-I	X	X_0	Y	Z
Y-type-II	X	Y	X_0	Z
Y-type-III	X_0	X	Y	Z

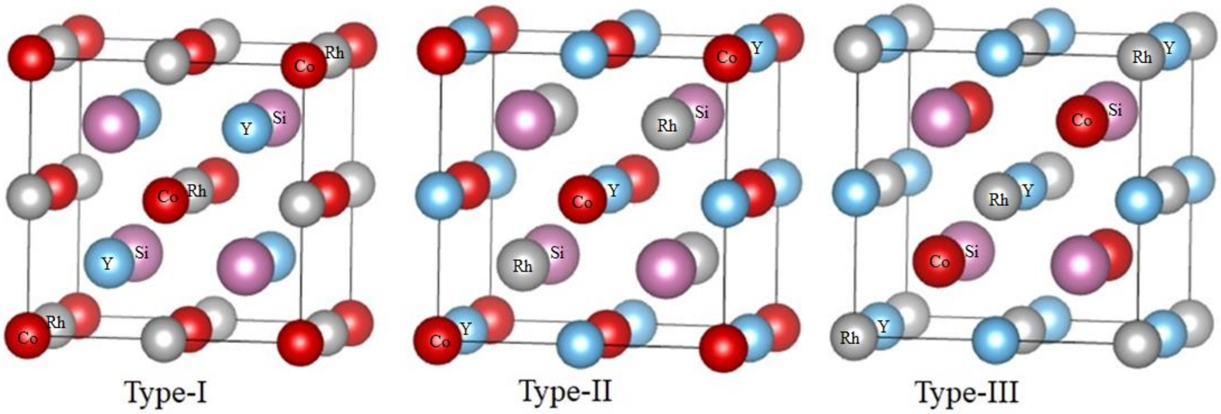

Figure 5.The three different types of the primitive cell of the quaternary Heusler compounds.

These Heusler compounds have shown interesting properties such as spin gapless semiconductor, half-metallic ferromagnetic, high curie temperature, and fine thermoelectric properties [12], [15], [53]–[55].

4.2 Details of the Calculations

Density functional theory (DFT), as implemented in VASP code [79], is used to do the calculations. 520 eV was chosen as the cut-off energy, while 10^{-8} eV was chosen as the total energy tolerance. For unit-cell structures, the formation energy was computed using a 22 x 22 x 22 Γ- centered k-point mesh. The phonopy package [80] was used to investigate dynamical stability using VASP code with 4 x 4 x 4 supercell structures and a 4 x 4x 4 Γ - centered k-point mesh. The total energy was then calculated using the full-potential linearized augmented plane wave (FP-LAPW) method implemented in WIEN2k code [81] using the optimized structural parameters acquired by VASP code [82]. The generalized gradient approximation of Perdew–Burke–Ernzerhof (GGA-PBE) [66] was used to treat the exchange–correlation potential. K_{max} R_{MT} = 9 was used to define the wavefunctions in the interstitial area, where R_{MT} is the smallest atomic muffin tin radius and K_{max} is the largest reciprocal lattice vector of the plane wave expansion. For Co, Cr, Mn, Rh, and Z (Z = Si) atoms, R_{MT} values of 2.4, 2.2, 2.0, and 1.7 atomic units (a.u.) were chosen, respectively. 10^{-4} Ry, 10^{-4} e, and 1 mRy/au were chosen as the total energy, charge density convergence tolerances, and force tolerances, respectively. These TE properties were calculated using DFT with a high-density mesh of 10,000 k-points, which is equivalent to a 36 x 36 x 36 centered k-mesh. The constant relaxation time approximation was used for the TE computations, which was set to 0.5 X 10^{-15} s.

4.3 Structural Properties

CoRhYSi (Y = Cr, Mn) QHAs have a stoichiometry of 1:1:1:1 and a chemical formula of XX′YZ, where X, X′, and Y are transition metal elements and Z is a main group element with s-p orbitals. The QHAs crystallize in a face-centered cubic LiMgPdSn (Y-type) structure with the space group F43m (no. 216). The atomic configurations of this sort of structure are Y-type-I, Y-type-II, and Y-type-III, as shown in Figure 1. The element's Wyckoff positions in the three types are 4a (0,0,0), 4c (1/4, 1/4, 1/4), 4b (1/2, 1/2, 1/2), and 4d (3/4, 3/4, 3/4), as shown in Table 2. The Y-type-I crystal structure was found to be the most stable crystal structure based on total energy calculations (see Table 3). The formation energy (E_{form}) is calculated using the following formula to determine the thermodynamic stability of these QHAs [83]:

$$E_{form} = E_{tot} - (E_{Co}^{bulk} + E_{Rh}^{bulk} + E_{Y}^{bulk} + E_{Z=Si}^{bulk}), \qquad \text{Equation 55}$$

where E_{tot} represents the equilibrium total energy per formula unit of CoCrRhSi, CoMnRhGe alloys, and E_{Co}^{bulk}, E_{Rh}^{bulk}, E_{Y}^{bulk}, and $E_{Z=Si}^{bulk}$ refer to the equilibrium total energies per atom in their individual bulk structures. Table 4 shows that the formation energy values are negative, indicating that CoYRhSi (Y = Cr, Mn) QHAs are thermodynamically stable. Table 4 also shows the optimized lattice parameter for each alloy. It is noticeable from this table that the increase in the atomic number of Z (Z = Si) atoms increases the lattice parameters. The calculated lattice parameter values are in agreement of the experimental results, see Table 4 [83]. It calculated the total energy as a function of volume of all three possible atomic configurations to determine the most stable structure, taking into account the paramagnetic (NM) and ferromagnetic (FM) phases [84]. It's worth noting that the majority of magnetic Heusler compounds are stable in their ferromagnetic state [84]. The equilibrium structural parameters can then be determined by minimizing the energy.

Table 2.The Wyckoff positions 4a, 4c, 4b, 4d of the atoms in CoYRhSi (Y = Cr, Mn) quaternary Heusler alloys for three types of configurations

Y	4a (0,0,0)	4b (1/2, 1/2, 1/2)	4c (1/4, 1/4, 1/4)	4d (3/4, 3/4, 3/4)
Type-I	Co	Rh	Y	Z
Type-II	Co	Y	Rh	Z
Type-III	Rh	Co	Y	Z

Table 3. The total energy in eV of CoYRhSi (Y = Cr, Mn) QHAs in the three types of configurations

Alloys	Type-I	Type-II	Type-III
CoCrRhSi	-29.719	-30.633	- 30.145
CoMnRhSi	- 29.187	-30.749	- 29.918

Table 4. Lattice constant a (Å), elastic constants C_{ij} (GPa), bulk modulus *B* (GPa), Young's modulus *E* (GPa), isotropic shear modulus *G* (GPa), Poisson's ratios *v*, anisotropy factor *A*, Pugh's ratio *B/G*, and the melting temperature T_{melt} (K) of CoRhYSi (Y = Mn, Cr) quaternary Heusler compounds

Physical parameter	CoCrRhSi	CoMnRhSi
$E_{form}(eV)$	-1.321	-1.914
a	5.786 5.786[a)]	5.839 5.839[c)]
C_{11}	335.898	334.408
C_{12}	145.233	141.947
C_{44}	58.916	72.14
B	216.881 234.569[b)]	211.453
E	185.233	216.135
G	68.357	81.295
v	0.358	0.330
A	0.618	0.749
C_p	86.317	69.0547
B/G	3.173	2.601
T_{melt}	2624	2574

a,b)Ref [84] c)[49]

4.4 Dynamical Phonon Properties

The structural stability of the energetically stable Y-type-I configuration of CoRhYSi (Y = Cr, Mn) alloys established in Section 4.3 is confirmed in this subsection. The phonon dispersion curves (PDCs) provide another indicator of the stability of the investigated alloys. It is clear from Figure 6 that these CoRhYSi alloys have positive frequencies (no imaginary modes), indicating that they are dynamically stable. As the primitive cell of CoRhYSi (Y = Mn, Cr) compounds has four atoms, the phonon dispersion curve contains twelve phonon branches. Three phonon modes are acoustic (one longitudinal acoustic (LA) and two transversals acoustic (TA)), and nine optical branches (three longitudinal optical (LO) and six transverse optical (TO)). The phonon frequencies of CoFeCrGe and CoFeTiGe quaternary Heusler alloys are in agreement with those obtained in previous calculations [84]. With the path of high symmetry points from $\Gamma\ to\ X$ and from $\Gamma\ to\ L$, the two transversal acoustic modes are degenerate. Therefore, the TA is the only one mode that appears in Figure 6 (a) and (b). Although, the two transverse acoustic modes are nondegenerate with the path $L - W\ and\ X - W$. For the other Heusler compounds, this degeneracy in these two transverse acoustic modes of the phonon dispersion was anticipated [85]. The long longitude optical phonon creates the polarization electric field and eventually reinforces the longitude force due to the Coulomb interaction caused by the charged vibrating atoms. As a result, the longitude optical phonon's frequency rises [57], [87], [88]. The varied contributions of the constituted atoms to the phonon density of states can be explained by the constituted atoms' different masses. Low frequency modes are contributed by heavy mass atoms, while high frequency modes are contributed by light mass atoms. The phonon dispersion curves of materials are also determined in terms of their dynamical stability. It is well known that materials are dynamically stable if their phonon dispersion curves contain no imaginary phonon modes [84]. The fact that there is no negative frequency in the figure indicates that the examined Heusler compound is dynamically stable.

The Y-type-II structure of CoRhYSi (Y = Mn, Cr) compounds are mechanically stable because the twelve phonon branches show positive frequencies. The phonon total density of state (TDOS) of CoRhYSi (Y = Mn, Cr) compounds are shown in Figure 7. Co and Si atoms manifest high contributions for both compounds at low frequency modes. However, the major contributions to the phonon TDOS come from Co, Cr, and Mn atoms for CoRhYSi.

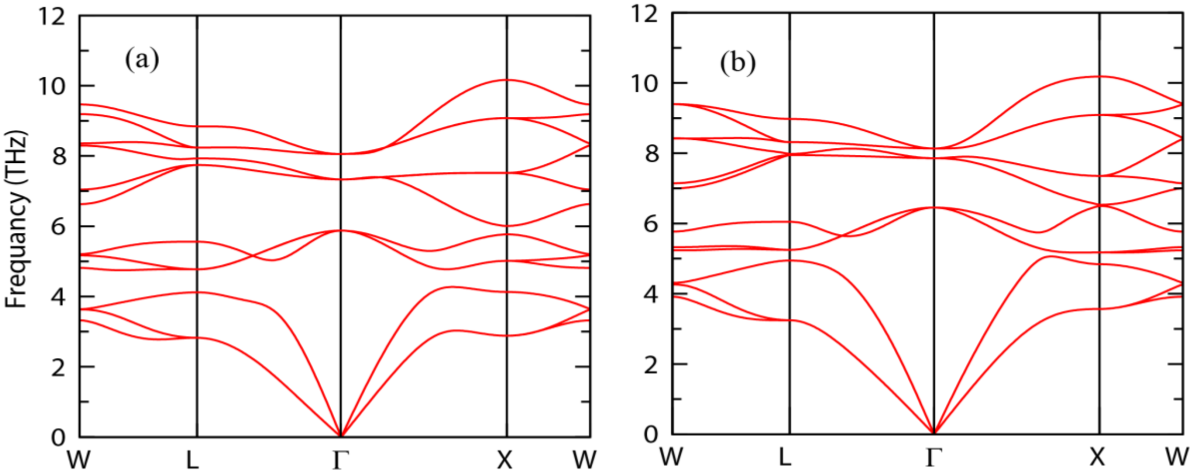

Figure 6. Phonon dispersion relation of (a) CoRhCrSi (b) CoRhMnSi quaternary Heusler compounds.

The lattice thermal conductivity (k_L) is linked to the efficiency of thermoelectric material where the proper thermoelectric generator should possess a low k_L value. The lattice thermal conductivity is written as the follow:

$$k_L^{\alpha\beta} = \frac{1}{k_B T^2 \Omega N} \sum_\lambda f_0(f_0 + 1)\,(\hbar\omega_\lambda)^2 v_\lambda^\alpha F_{\lambda,}^\beta \qquad \text{Equation 56}$$

where Ω is the volume of the unit cell, N is the number of q-points, f_0 is the phonon distribution function at thermal equilibrium, v_λ is the group velocity, ω_λ is the angular frequency of phonon mode (λ), and $\alpha\ and\ \beta$ are scattering directions. The difference of the lattice thermal conductivity with the temperature is shown in Figure 9. The lattice thermal conductivity as a function of temperature. The values of the lattice thermal conductivity at the room temperature are 1.84 $Wm^{-1}K^{-1}$ and 2.951 $Wm^{-1}K^{-1}$for CoCrRhSi and CoMnRhSi alloys, respectively. The different k_L values of CoCrRhSi and CoMnRhSi compounds is related to the difference in molars masses of Cr and Mn atoms. Also, since they have a huge difference of molars masses between the atoms in the compound, there is a gap between the acoustic and the optical modes, which conducts to greater phonon relaxation times and thus greater k_L values [86], and that show the possible reason for the low k_L of CoRhYSi (Y = Mn, Cr) where there is not any gap between the acoustic and the optical phonon modes in Figure 6. Thus, the low lattice thermal conductivity of CoRhYSi (Y = Mn, Cr) compounds suggest these alloys as good candidates for thermoelectric applications at high temperatures.

To the lattice thermal conductivity, the acoustic modes express the high contribution, since the optical modes have low phonon group velocity. There are many materials exhibit similar behavior [90]–[92]. Reducing lattice thermal conductivity, can be utilized form these results. The Cr and Mn atoms are the main source of contribution to the optical modes. Thus, reducing in k_L and increasing in figure of merit comes from the generating vacancies at the (Y = Mn, Cr) atoms.

4.5 Mechanical Properties

The mechanical properties of the alloys are examined to confirm their mechanical stability. As CoRhYSi (Y = Mn, Cr) alloys have a cubic structure, they only have three independent elastic constants: longitudinal compression (C_{11}), transverse expansion (C_{12}), and the share modulus predictor (C_{44}). The mechanical stability was investigated for the three structure types of CoRhYSi (Y = Mn, Cr) quaternary Heusler Compounds as presented in Table 1. From the three types and their structure, the Y-type-II was the most stable structure.

The mechanical stability was investigated using the Born-Hanung conditions, which are given as [91]:

$(C_{11} - C_{12})/2 > 0$ Equation 57

$(C_{11} + 2C_{12})/3 > 0$ Equation 58

$B > 0$ Equation 59

$C_{12} < B < C_{11}$ Equation 60

$C_{44} > 0$ Equation 61

Here, C_{11}, C_{12} and C_{44} represent the three independent elastic constants. These values of the elastic constant satisfy the Born-Haung criteria. Thus, the second type (T-type-II) structure of CoRhYSi (Y = Mn, Cr) quaternary Heusler compounds is mechanically stable. The bulk modulus (*B*), shear modulus (*G*), Young's modulus (*E*), Cauchy pressure (Cp), Poisson's ratio (*v*), Pugh's ratio (*B/G*), and anisotropy factor (*A*) are given in Table 4. The mechanical properties were obtained using the calculated elastic as follows [92]–[95]:

$B = (C_{11} + 2C_{12})/3$ Equation 62

$G = (G_V + G_R)/2$ Equation 63

$G_R = \frac{5C_{44}(C_{11}-C_{12})}{4C_{44}+3(C_{11}-C_{12})}$ Equation 64

$G_V = \frac{C_{11}-C_{12}+3C_{44}}{5}$ Equation 65

$E = 9BG/(3B + G)$ Equation 66

$v = (3B - 2G)/2(3B + G)$ Equation 67

$A = 2C_{44}/(C_{11} - C_{12})$ Equation 68

$C_p = C_{12} - C_{44}$ Equation 69

Where G_R is Reuss's Shear modulus, and G_V is Voigt's shear modulus [92]–[95]. The values of the bulk modulus of CoCrRhSi and CoMnRhSi quaternary Heusler compounds are in agreement with the previous theoretical results, see Table 4. The value of bulk modulus of CoMnRhSi is smaller than the CoCrRhSi, and that shows the latter compound has a higher resistance to compression. Young modulus values, E, are 185.233 and 216.135 GPa for CoCrRhSi and CoMnRhSi, respectively. The E and G values of CoMnRhSi are higher than those of CoCrRhSi. This means that CoMnRhSi compound is harder than CoCrRhSi and the shear force causes larger lateral deformation. The hardness of a material is determined by its bulk modulus and shear modulus. The fact that the bulk modulus is much bigger than the shear modulus indicates that the material is more resistant to uniaxial strain than to shear deformation, which is consistent with the previous findings [84].

Poisson's ratio is the transverse extension to the axial contraction. The Poisson's ratio of CoCrRhSi is higher than that of CoMnRhSi. The anisotropy factor (*A*) value is a measure of the material's anisotropy [96]. Isotropic materials have *A* = 1, but anisotropic materials have A values less than or greater than 1 [69]. Both CoCrRhSi and CoMnRhSi have *A* values less than one, which indicate anisotropic materials (see Table 4). The material is considered ductile if it has a B/G value greater than 1.75 [97]. The ductility and brittleness of materials are described using Pugh's ratio (B/G) and Cauchy pressure (C_p). The materials are ductile (brittle) in nature if B/G is greater (less) than 1.75 [98]. The ductility and brittleness of materials are described using Pugh's ratio (B/G) and Cauchy pressure (C_p). The materials are ductile (brittle) in nature if B/G is greater than 1.75 [99]. In Table 4, the two compound CoCrRhSi and CoMnRhSi have a high Pugh's ratios (B/G) 3.173 and 2.601 respectively, so the compounds are considered ductile. Pugh's ratio is found by calculating the bulk and shear moduli [100]. Furthermore, if the C_p value is positive (negative), the material is ductile (brittle) by nature [99]. Furthermore, the Cauchy pressure (C_p) values for CoCrRhSi and CoMnRhSi are 86.317, and 69.0547 GPa, respectively.

The B/G ratio is found to be more than 1.75, and Cp values are positive, indicating that these alloys are ductile. Similar QHAs, such as CoFeYGe (Y = Ti, Cr) [85], have similar results.

Another essential quantity is the melting temperature, which provides information on the material's heat resistance and may be determined using the formula [99], [101], [102]:

$$T_{melt} = \left[553\ K + \left(\frac{5.91\ K}{GPa}\right) C_{11}\right] \pm 300\ K \qquad \text{Equation 70}$$

This equation shows that the melting temperature is depending on the bulk modulus value. Therefore, if the material with higher bulk modulus has higher melting temperature as shown in Table 4. CoCrRhSi and CoMnRhSi alloys have melting points of 2624 K, and 2547 K, respectively. The high melting temperatures, T_{melt}, indicate that these QHAs are mechanically stable within a $\pm 300\ K$ range. The calculations demonstrate that the alloys with lower longitudinal compression (C_{11}) have lower melting points (see Table 4), which are comparable to those of CoFeCrGe (2584 K) and CoFeTiGe (2484 K) [85]. The ratio of reflected wave energy to incident wave energy at a material's surface is known as the reflective index [100].

4.6 Electronic and Magnetic Properties

The band structure, total density of states (TDOS), projected density of states (PDOS), and magnetic characteristics of CoRhYSi (Y = Mn, Cr), quaternary Heusler alloys are presented in this section. The band structure and TDOS of CoRhYSi (Y = Mn, Cr), alloys are shown in Figure 7. For CoRhYSi (Y = Mn, Cr) quaternary Heusler compounds, the spin polarized band structure was calculated along the high symmetry paths of the first Brillouin zone. From Figure 7, the CoRhYSi (Y = Mn, Cr) alloys were found that they have half-metallic behavior. The minority spin channel in these structures behaves as semiconducting, with band gap values of 0.542 and 0.576 eV along the Γ and X symmetry line, respectively, whereas the majority spin channel behaves metallically. The positive and negative values correspond to the DOS of the spin-up and spin-dn states, respectively. The hybridized state of Cr, Mn, and Rh as they cross the Fermi level is responsible for the metallic behavior in the spin-up channel [84]. The separation between these anti-bonding states forms the spin-dn semiconducting band gap, as seen in several EQH compounds [56], [103].

From Equation 1, the electric spin polarization of CoRhYSi (Y = Mn, Cr) quaternary Heusler compounds was calculated at the Fermi energy. CoRhYSi (Y = Mn, Cr) quaternary Heusler compounds express a 100% electron spin polarization due to the absence of minority-spin density of state at E_f. Thus, these compound are showing a promising materials for spintronic application [85]. At Γ and X, the Valence band maximum (VBN) and the conduction band minimum (CBN) are located, respectively, and the Fermi energy is near (VBN). Therefore, CoCrRhSi and CoMnRhSi reveal an indirect band gap of 0.542 eV and 0.576 eV, respectively, in the minority-spin channel. These results are in agreement with the other studies as follow in Table 4. These results are consistent with previous ab initio investigations of CoFeCuZ quaternary Heusler alloys (Z = Al, As, Ga, In, Pb, Sb, Si, Sn) [85]. Furthermore, the occurrence of flat energy levels in the conduction bands along the Γ and X symmetry line, as well as significantly dispersive bands in other directions, could indicate a high Seebeck coefficient and thermoelectric properties [99].

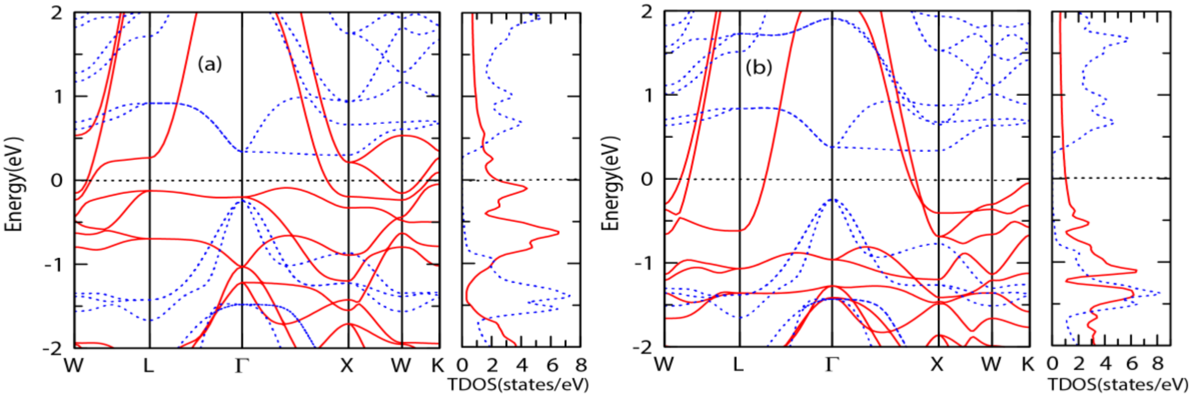

Figure 7. The electronic band structures and total density of states (TDOS) of a) CoCrRhSi, b) CoMnRhSi The solid and dotted lines represent the majority and minority spin channels, respectively.

The following formula can be used to calculate the spin-polarization [104]:

$$P = \frac{\rho_{\uparrow}(E_f) - \rho_{\downarrow}(E_f)}{\rho_{\uparrow}(E_f) + \rho_{\downarrow}(E_f)}\ X\ 100 \qquad \text{Equation 71}$$

where $\rho_{\uparrow}(E_f)$ and $\rho_{\downarrow}(E_f)$ are the majority and minority spin density of states, respectively, at the Fermi level (E_f) [104]. Table 4 shows that the CoCrRhSi and CoMnRhSi alloys have a perfect spin-polarization of 100 percent, corresponding to half-metallic behavior. CoFeMnGe QHAs have a similar high spin-polarization value [19].

Table 5. The calculated band gap values E_g (eV), spinpolarization P (%), total magnetic moment Mtotal (μB), local magnetic moments per atom M_i (μB) (i = Co, Cr, Mn Rh, Z) for CoRhYZ (Y = Cr,Mn) (Z = Si) alloys

Compound	E_g(eV)	P (%)	m_{Co} $[\mu_B]$	$m_{Rh}[\mu_B]$	$m_Y[\mu_B]$	$m_{Si}[\mu_B]$	m_{total} $[\mu_B]$
CoRhCrSi	0.54 (minority)	100	1.15	0.36	2.41	-0.02	4.00
					2.390 b)		4.00 a)
CoRhMnSi	0.57 (minority)	100	1.25	0.44	3.31	-0.02533	5.00

a, b) [84]

In Table 5, the calculated local and total magnetic moments under the equilibrium lattice constant of CoRhYSi (Y = Mn, Cr) compounds are given. CoCrRhSi compound displays a ferromagnetic behavior, that is appeared from the total magnetic moment of 4.00 μ_B. Also, CoMnRhSi compound expresses a ferromagnetic behavior with total magnetic moment of 5.00 μ_B. From the local magnetic moments of Cr, Mn and Co atoms, the major benefaction comes of the total magnetic moment of CoCrRhSi and CoMnRhSi. To the total magnetic moments, the metalloid atom (Si) reveals a negligible contribution. The half-metallicity of material is stated by the Slater-Pauling rule, and its total magnetic moment. Also, the half-metallic behavior is depending in the integer value of total magnetic moment. For the CoRhYSi (Y = Mn, Cr) compounds, the Slater-Pauling rule is given by the following equation [105], [106]:

$$M_{tot} = (Z_{tot} - 20)\mu_B \qquad \text{Equation 72}$$

Where M_{tot} is the total magnetic moment, and Z_{tot} is the accumulated number of valence electrons. The integer values of 4.00 and 5.00 μ_B for CoRhYSi (Y = Mn, Cr) alloys are shown in this table 5, confirming the half-metallic behavior of these QHAs. As a result, these QHAs appear to be potential candidates for future spintronic applications [107]. In the cases of CoCrRhSi and CoMnRhSi alloys, however, the Cr and Mn atoms have local magnetic moments of 2.41 and 3.31 μ_B, respectively. In the case of CoCrRhSi and CoMnRhSi alloys, the coupling between the local magnetic moments of Cr and Mn atoms and those of Co and Rh atoms is ferromagnetic. Rh atoms in CoCrRhSi and CoMnRhSi, with local magnetic values of 0.36 and 0.44 μ_B, respectively. The linear relationship between Curie temperature (TC) and total magnetic moments is acknowledged to be one of the methods that has been used to estimate the Curie temperature [83], [99], [108], [109]:

$$T_C = 23 + 181M_{tot} \qquad \text{Equation 73}$$

The value of Curie temperature for CoCrRhSi and CoMnRhSi alloys is found to be 747 and 928 K, respectively.

4.7 Thermoelectric Properties

By using the Boltzmann’s transport theory with constant relaxation time approximation, the thermoelectric properties of CoRhYSi (Y = Mn, Cr) quaternary Heusler compounds were examined [100], [110]. Predicting the electronic transport properties by this method of approximation showed good results comparing with the experimental measurements [111]–[114]. To calculate the thermoelectric properties, the constant relaxation time of $\tau \sim 0.5\ X\ 10^{-15}\ s$ was used Similar systems, such as FeRhCrSi and FeRhCrGe QHAs, were also examined [115]. When the materials have a narrow band gap, they could have a great efficiency to transform the heat to electricity [116]. These alloys were observed to have small band gaps of 0.542 eV and 0.576 eV in the majority spin channel, making them particularly promising for thermoelectric applications. A semiconductor with a narrow band gap is assumed to have high thermoelectric properties [117]–[119]. The Seebeck coefficient (S) and the electrical conductivity (σ) are depending in the spin in the half-metallic material.

The following equations are used to compute the Seebeck coefficient (S), electrical conductivity (σ), and electronic thermal conductivity (k_e) [120]:

$$\sigma_{\alpha\beta}(T,\mu) = \frac{1}{\Omega}\int \sigma_{\alpha\beta}(\varepsilon)\left[-\frac{\partial f_{\mu}(T,\epsilon)}{\partial\varepsilon}\right]d\varepsilon \qquad \text{Equation 74}$$

$$k_{\alpha\beta}(T,\mu) = \frac{1}{e^{2}T\Omega}\int \sigma_{\alpha\beta}(\varepsilon)(\varepsilon-\mu)^{2}\left[-\frac{\partial f_{\mu}(T,\epsilon)}{\partial\varepsilon}\right]d\varepsilon \qquad \text{Equation 75}$$

$$S_{\alpha\beta}(T,\mu) = \frac{1}{eT\Omega\sigma_{\alpha\beta}(T,\mu)}\int \sigma_{\alpha\beta}(\varepsilon)(\varepsilon-\mu)\left[-\frac{\partial f_{\mu}(T,\epsilon)}{\partial\varepsilon}\right]d\varepsilon \qquad \text{Equation 76}$$

$$\sigma_{\alpha\beta} = \frac{e^{2}}{N_k}\sum_{i,k}\tau\, v_{\alpha}(i,k)v_{\beta}(i,k)\frac{\delta(\varepsilon-\varepsilon_{i,k})}{d\varepsilon} \qquad \text{Equation 77}$$

Where σ is the electrical conductivity, k_e is the electric thermal conductivity, S is the Seebeck coefficient, α and β are tensor components, and $\Omega, v, and\ N_k$ are the chemical potential.

The total Seebeck coefficient and electrical conductivity of the majority and minority spin channels were calculated using the two-current model, as shown in [121]:

$$S = (S_{\uparrow}\sigma_{\uparrow} + S_{\downarrow}\sigma_{\downarrow})/\sigma_{\uparrow} + \sigma_{\downarrow} \qquad \text{Equation 78}$$

Where $(\uparrow)\ and\ (\downarrow)$ are the spin-up and spin-down channels, and the σ_{total} is the total electrical conductivity that is written as [121]:

$$\sigma_{total} = (\sigma_{\uparrow} + \sigma_{\downarrow}) \qquad \text{Equation 79}$$

The Seebeck coefficient of spin-up and spin-down channels and the total S as a function of the chemical potential at 300 K and 800 K show in Figure 8 (a), (b). The total Seebeck coefficient values increase as the temperature goes up, as can be seen in this graph. The highest values of S for the CoCrRhSi and CoMnRhSi alloys are achieved at 800 K, with values of 7.86976 $\mu V/K$ and 37.6746 $\mu V/K$, respectively. At 300 K and 800 K, Figure 8 (c), (d) shows the electrical conductivity (σ) as a function of the chemical potential. The electrical conductivity of the n-type is found to be higher than that of the p-type. Furthermore, the impact of temperature on values is shown to be minimal. Additionally, Figure 8 (e), (f) indicates that k_e behaves similarly to σ (n-type k_e values are higher than p-type k_e values). The direct relationship between electrical conductivity and electronic thermal conductivity (k_e), which is approximated by the Wiedemann–Franz equation $(k_e = L\sigma T)$ is responsible for this [100]. Therefore, as the temperature goes up, the ke values increase as well. The power factor (PF) is shown in Fig. 5 (g), (h), with the values increasing as the temperature increases. At 800 K, the maximum PF values for CoCrRhSi and CoMnRhSi alloys are 20.2596 X 10^{11}, and 31.1445 X 10^{11} $Wm^{-1}K^{-2}$, respectively. The lattice thermal conductivity (kl) of the investigated alloys was computed using Slack's equation, which is one of the most accurate techniques for computing kl value, as follows [122]–[125]:

$$K_l = A\frac{\bar{M}\Theta_D^3 V^{1/3}}{\gamma^2 n^{2/3} T} \qquad \text{Equation 80}$$

$$A = \frac{2.43X10^{-6}}{1-\frac{0.514}{\gamma}+\frac{0.228}{\gamma^2}} \qquad \text{Equation 81}$$

Where A, $\bar{M}, \Theta, V, \gamma, n, T$ and T are the average atomic mass, Debye temperature, volume per atom, Grüneisen parameter, number of atoms in the primitive unit cell, and temperature, respectively [125]. The Debye temperature and the Grüneisen parameter are derived using the following formulae based on the elastic constant computations [125], [126]:

$$\Theta_D = \frac{h}{k_B}(\frac{3n\rho N_A}{4\pi M})^{1/3} v_m$$

Equation 82

$$v_m = [\frac{1}{3}(\frac{2}{v_t^3} + \frac{1}{v_t^3})]^{-1/3}$$

Equation 83

$$v_t = \sqrt{\frac{G}{\rho}}$$

Equation 84

$$\gamma = \frac{9-12(v_t/v_t)^2}{2+4(v_t/v_t)^2}$$

Equation 85

The Planck constant, density, Avogadro's number, Boltzmann constant, and molecular weight are represented by the constants h, ρ, N_A, K_{lB}, and M, respectively, whereas v_m, v_l, and v_t are the average, transverse, and longitudinal sound velocities, respectively. Table 6 shows that the Debye temperatures of CoCrRhSi and CoMnRhSi alloys are 420.78573K, and 454.28902 K, respectively. This table shows that decreasing the average sound velocities lowers the Debye temperature, which is consistent with previous computations by Co2MnAl, Co2MnGa, and Co2MnIn [101]. A high Debye temperature indicates that the material is hard, whereas low values are noticeable in soft materials [84].

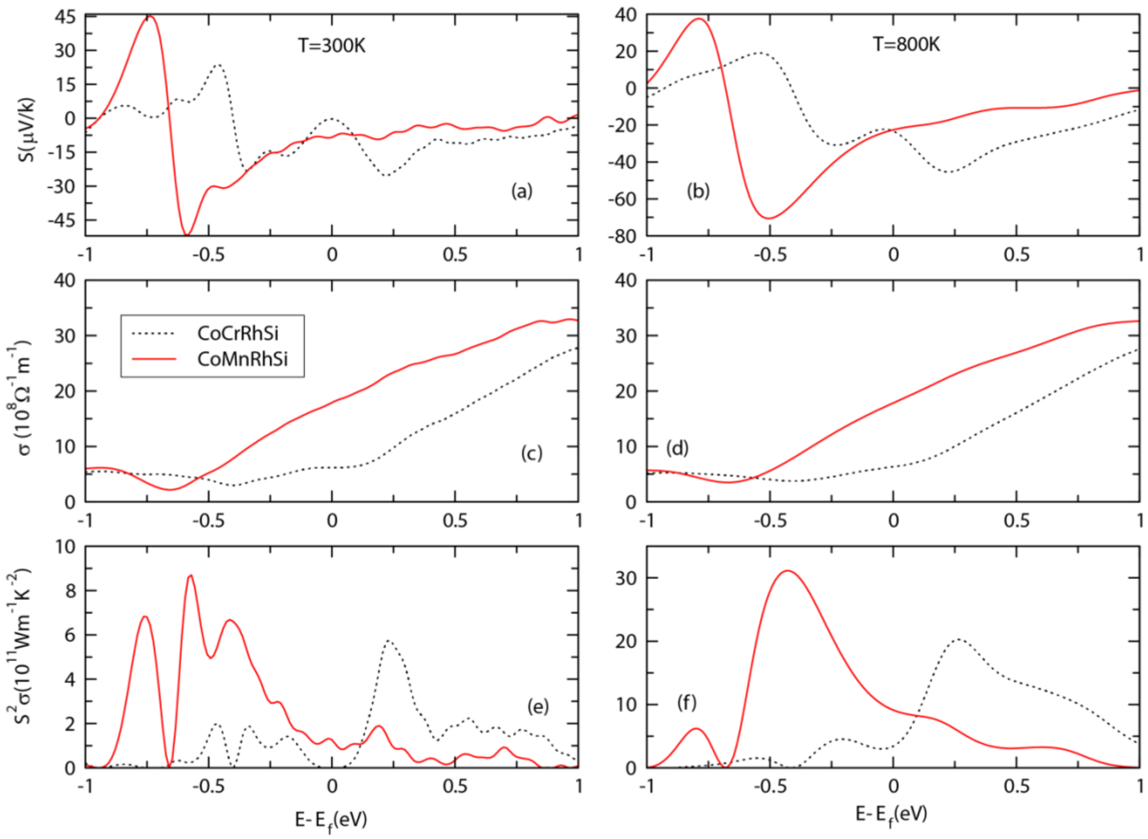

Figure 8. a, b the Seebeck coefficient (S), c, d electrical conductivity (σ), and e, f power factor PF ($S^2\sigma$) as a function of the chemical potential at temperatures of (300 K, 800 K) for CoRhYSi (Y = Mn, Cr) QHAs.

Table 6.The Debye temperature Θ_D (K), average sound velocity v_m (m/s), transverse sound velocity v_t (m/s), longitudinal sound velocity v_l (m/s), density ρ (kg/m3), and Grüneisen parameter γ for CoRhYSi (Y = Mn, Cr) QHAs.

Alloys	Θ_D	v_m	v_t	v_l	ρ	γ
CoCrRhSi	420.78573	3274.84773	2909.84588	6176.90820	8186.08620	2.19
CoMnRhSi	454.28902	3533.46082	3151.32506	6250.75660	8073.10299	1.97

Using the aforementioned values, the lattice thermal conductivity (K_l) was calculated (see Figure 9). The lattice thermal conductivity of CoRhYSi (Y = Mn, Cr) alloys declines as temperature rises, as seen in this graph. At 300 K, the lattice thermal conductivity of CoCrRhSi and CoMnRhSi is 1.84065 and 2.95174 $Wm^{-1}K^{-1}$, respectively, and at 800 K, the lattice thermal conductivity of CoCrRhSi and CoMnRhSi is 0.690245 and 1.1069 $Wm^{-1}K^{-1}$, respectively. At 300 K, these values are lower than related structures like CoFeCrGe (11.01$Wm^{-1}K^{-2}$) and CoFeTiGe (12.26 $Wm^{-1}K^{-2}$) [85]. Figure 10 shows the figure of merit ZT values as a function of chemical potential at 300 and 800 K. At 800 K, CoRhYSi (Y = Mn, Cr) alloys have greater ZT values, as shown in this figure 9. At 800 K, CoCrRhSi and CoMnRhSi have the highest n-type ZT values of 0.838235 and 2.04368 eV. respectively. These ZT values are greater than recent calculations of 0.45 eV and 0.41 eV for FeRhCrSi and FeRhCrGe QHAs, respectively, at 800 K [115].

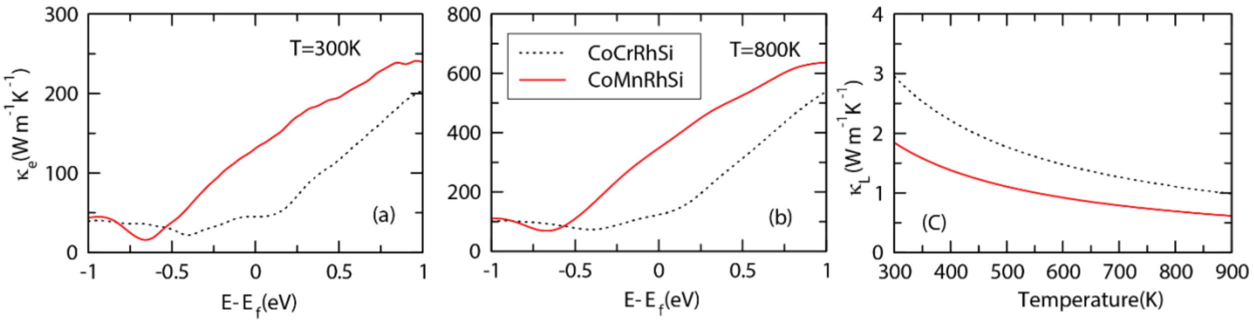

Figure 9. a, b electronic thermal conductivity (κe) and the lattice thermal conductivity (K_l) as a function of the temperature for CoRhYSi (Y = Mn, Cr)) as a function of the chemical potential at (300 K, 800 K) for CoRhYSi (Y = Mn, Cr) alloys

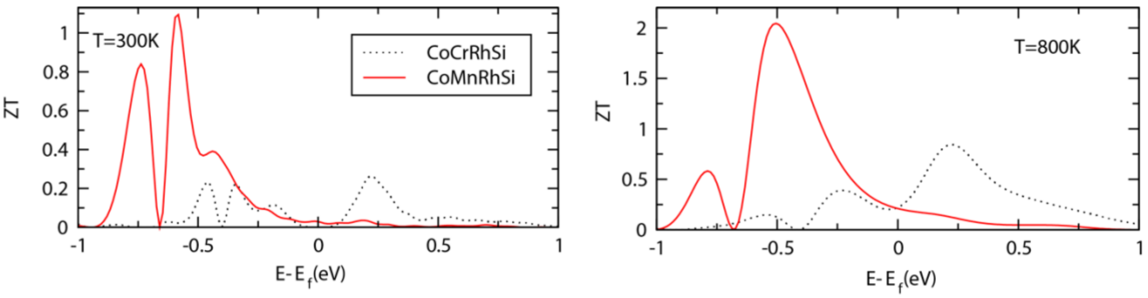

Figure 10. the figure of merit (ZT) as a function of the chemical potential at (300 K, 800 K) for CoRhYSi (Y = Mn, Cr) alloys

Chapter 5: Conclusion

DFT computations are used to investigate the structural, thermodynamic, dynamical, mechanical, electronic, magnetic, and thermoelectric properties of CoRhYSi (Y = Mn, Cr) quaternary Heusler alloys. The Y-Type-II structure was found to be the most stable configuration for these QHAs based on total energy calculations. These CoCrRhSi and CoMnRhSi alloys exhibit half-metallic behavior with band gaps of 0.542 and 0.576 eV, respectively. With an integer total magnetic moments of 4.00 and 5.00 μ_B and a spin-polarization of 100 %, they show half-metallic ferromagnetic properties. Because of their half-metallic ferromagnetic properties, they appear to be good candidates for spintronic applications. CoRhYSi (Y = Mn, Cr) QHAs have good thermoelectric properties, according to calculations utilizing the semiclassical Boltzmann transport theory within the constant relaxation time approximation. At 800 K, the maximum values of the power factor for CoCrRhSi and CoMnRhSi QHAs, respectively, are 20.2596 X 10^{11}, and 31.1445 X 10^{11} $Wm^{-1}K^{-2}$. The calculations predict that n-type CoCrRhSi and CoMnRhSi have the highest ZT values of of 0.84 and 2.04, respectively, whereas CoMnRhSi has the highest p-type ZT value of 2.04 at 800 K. As a result, these alloys have the potential to be used in thermoelectric applications at high temperatures.

References

[1] C. Haddad, C. Périlhon, A. Danlos, M.-X. François, and G. Descombes, “Some efficient solutions to recover low and medium waste heat: competitiveness of the thermoacoustic technology,” *Energy Procedia*, vol. 50, pp. 1056–1069, 2014.

[2] J. Yang and F. R. Stabler, “Automotive applications of thermoelectric materials,” *J. Electron. Mater.*, vol. 38, no. 7, p. 1245, 2009.

[3] L. E. Bell, “Cooling, heating, generating power, and recovering waste heat with thermoelectric systems,” *Science*, vol. 321, no. 5895, pp. 1457–1461, 2008.

[4] J. R. Sootsman, D. Y. Chung, and M. G. Kanatzidis, “New and old concepts in thermoelectric materials,” *Angew. Chem. Int. Ed.*, vol. 48, no. 46, pp. 8616–8639, 2009.

[5] A. Montecucco, J. Buckle, and A. Knox, “Solution to the 1-D unsteady heat conduction equation with internal Joule heat generation for thermoelectric devices,” *Appl. Therm. Eng.*, vol. 35, pp. 177–184, 2012.

[6] J. Yang and T. Caillat, “Thermoelectric materials for space and automotive power generation,” *MRS Bull.*, vol. 31, no. 3, pp. 224–229, 2006.

[7] R. Goldstein *et al.*, “Heat transfer—A review of 2004 literature,” *Int. J. Heat Mass Transf.*, vol. 53, no. 21–22, pp. 4343–4396, 2010.

[8] X. Liu, C. Li, Y. Deng, and C. Su, “An energy-harvesting system using thermoelectric power generation for automotive application,” *Int. J. Electr. Power Energy Syst.*, vol. 67, pp. 510–516, 2015.

[9] Z. Liu, C. Davis, W. Cai, L. He, X. Chen, and H. Dai, “Circulation and long-term fate of functionalized, biocompatible single-walled carbon nanotubes in mice probed by Raman spectroscopy,” *Proc. Natl. Acad. Sci.*, vol. 105, no. 5, pp. 1410–1415, 2008.

[10] C. Felser, G. H. Fecher, and B. Balke, “Spintronics: a challenge for materials science and solid-state chemistry,” *Angew. Chem. Int. Ed.*, vol. 46, no. 5, pp. 668–699, 2007.

[11] D. Jung, H.-J. Koo, and M.-H. Whangbo, “Study of the 18-electron band gap and ferromagnetism in semi-Heusler compounds by non-spin-polarized electronic band structure calculations,” *J. Mol. Struct. THEOCHEM*, vol. 527, no. 1–3, pp. 113–119, 2000.

[12] K. Özdoğan, E. Şaşıoğlu, and I. Galanakis, “Slater-Pauling behavior in LiMgPdSn-type multifunctional quaternary Heusler materials: Half-metallicity, spin-gapless and magnetic semiconductors,” *J. Appl. Phys.*, vol. 113, no. 19, p. 193903, 2013.

[13] Y. Sutou *et al.*, “Magnetic and martensitic transformations of NiMnX (X= In, Sn, Sb) ferromagnetic shape memory alloys,” *Appl. Phys. Lett.*, vol. 85, no. 19, pp. 4358–4360, 2004.

[14] F. Heusler, “Über Manganbronze und über die Synthese magnetisierbarer Legierungen aus unmagnetischen Metallen,” *Angew. Chem.*, vol. 17, no. 9, pp. 260–264, 1904.

[15] L. Bainsla, M. M. Raja, A. Nigam, and K. Suresh, “CoRuFeX (X= Si and Ge) Heusler alloys: High TC materials for spintronic applications,” *J. Alloys Compd.*, vol. 651, pp. 631–635, 2015.

[16] S. Wurmehl, G. H. Fecher, H. C. Kandpal, V. Ksenofontov, C. Felser, and H.-J. Lin, “Investigation of Co 2 Fe Si: The Heusler compound with highest Curie temperature and magnetic moment,” *Appl. Phys. Lett.*, vol. 88, no. 3, p. 032503, 2006.

[17] K. Kroth, B. Balke, G. H. Fecher, V. Ksenofontov, C. Felser, and H.-J. Lin, “Diluted magnetic semiconductors with high Curie temperature based on C 1 b compounds: Co Ti 1−x Fe x Sb,” *Appl. Phys. Lett.*, vol. 89, no. 20, p. 202509, 2006.

[18] L. Bainsla *et al.*, “High spin polarization in CoFeMnGe equiatomic quaternary Heusler alloy,” *J. Appl. Phys.*, vol. 116, no. 20, p. 203902, 2014.

[19] L. Bainsla *et al.*, “Spin gapless semiconducting behavior in equiatomic quaternary CoFeMnSi Heusler alloy,” *Phys. Rev. B*, vol. 91, no. 10, p. 104408, 2015.

[20] L. Bainsla *et al.*, “High spin polarization and spin splitting in equiatomic quaternary CoFeCrAl Heusler alloy,” *J. Magn. Magn. Mater.*, vol. 394, pp. 82–86, 2015.

[21] L. Bainsla *et al.*, “Origin of spin gapless semiconductor behavior in CoFeCrGa: Theory and Experiment,” *Phys. Rev. B*, vol. 92, no. 4, p. 045201, 2015.

[22] T. M. Bhat and D. C. Gupta, “First-principles study of high spin-polarization and thermoelectric efficiency of ferromagnetic CoFeCrAs quaternary Heusler alloy,” *J. Magn. Magn. Mater.*, vol. 449, pp. 493–499, 2018.

[23] X. Dong *et al.*, “Spin injection from the Heusler alloy Co 2 MnGe into Al 0.1 Ga 0.9 As∕ GaAs heterostructures,” *Appl. Phys. Lett.*, vol. 86, no. 10, p. 102107, 2005.

[24] S. Chadov *et al.*, “Efficient spin injector scheme based on Heusler materials,” *Phys. Rev. Lett.*, vol. 107, no. 4, p. 047202, 2011.

[25] Y. Sakuraba *et al.*, “Giant tunneling magnetoresistance in Co 2 Mn Si∕ Al–O∕ Co 2 Mn Si magnetic tunnel junctions,” *Appl. Phys. Lett.*, vol. 88, no. 19, p. 192508, 2006.

[26] B. Hamad, “Ab initio investigations of the structural, electronic, and thermoelectric properties of Fe 2 NbAl-based alloys,” *J. Mater. Sci.*, vol. 51, no. 24, pp. 10887–10896, 2016.

[27] G. Joshi and B. Poudel, “Efficient and robust thermoelectric power generation device using hot-pressed metal contacts on nanostructured half-Heusler alloys,” *J. Electron. Mater.*, vol. 45, no. 12, pp. 6047–6051, 2016.

[28] C. Fu *et al.*, “Realizing high figure of merit in heavy-band p-type half-Heusler thermoelectric materials,” *Nat. Commun.*, vol. 6, no. 1, pp. 1–7, 2015.

[29] O. Heusler, “Kristallstruktur und Ferromagnetismus der Mangan-Aluminium-Kupferlegierungen,” *Ann. Phys.*, vol. 411, no. 2, pp. 155–201, 1934.

[30] K. Özdog and I. Galanakis, “First-principles electronic and magnetic properties of the half-metallic antiferromagnet Cr2MnSb,” *J. Magn. Magn. Mater.*, vol. 321, no. 15, pp. L34–L36, 2009.

[31] J. Drews, U. Eberz, and H.-U. Schuster, “Optische Untersuchungen an farbigen Intermetallischen phasen,” *J. Common Met.*, vol. 116, no. 1, pp. 271–278, 1986.

[32] W. Jeitschko, “Transition metal stannides with MgAgAs and MnCu 2 Al type structure,” *Metall. Trans.*, vol. 1, no. 11, pp. 3159–3162, 1970.

[33] V. Alijani *et al.*, “Electronic, structural, and magnetic properties of the half-metallic ferromagnetic quaternary Heusler compounds CoFeMn Z (Z= Al, Ga, Si, Ge),” *Phys. Rev. B*, vol. 84, no. 22, p. 224416, 2011.

[34] G. Gao, L. Hu, K. Yao, B. Luo, and N. Liu, “Large half-metallic gaps in the quaternary Heusler alloys CoFeCrZ (Z= Al, Si, Ga, Ge): A first-principles study,” *J. Alloys Compd.*, vol. 551, pp. 539–543, 2013.

[35] A. Amudhavalli, R. Rajeswarapalanichamy, and K. Iyakutti, “First principles study on Fe based ferromagnetic quaternary Heusler alloys,” *J. Magn. Magn. Mater.*, vol. 441, pp. 21–38, 2017.

[36] D. Johnson, K. Suresh, and A. Alam, “Half-metallic Co-based quaternary Heusler alloys for spintronics: Defect-and pressure-induced transitions and properties,” *Phys. Rev. B*, vol. 94, no. 18, p. 184102, 2016.

[37] X. Dai, G. Liu, G. H. Fecher, C. Felser, Y. Li, and H. Liu, “New quarternary half metallic material CoFeMnSi,” *J. Appl. Phys.*, vol. 105, no. 7, p. 07E901, 2009.

[38] T. Graf, S. S. P. Parkin, and C. Felser, “Heusler Compounds-A Material Class With Exceptional Properties,” *IEEE Trans. Magn.*, vol. 47, no. 2, pp. 367–373, 2011, doi: 10.1109/TMAG.2010.2096229.

[39] H. Luo *et al.*, “Slater–Pauling behavior and half-metallicity in Heusler alloys Mn2CuZ (Z= Ge and Sb),” *Comput. Mater. Sci.*, vol. 50, no. 11, pp. 3119–3122, 2011.

[40] S. Skaftouros, K. Özdoğan, E. Şaşıoğlu, and I. Galanakis, “Generalized Slater-Pauling rule for the inverse Heusler compounds,” *Phys. Rev. B*, vol. 87, no. 2, p. 024420, 2013.

[41] G. Mahan, “Figure of merit for thermoelectrics,” *J. Appl. Phys.*, vol. 65, no. 4, pp. 1578–1583, 1989.

[42] G. J. Snyder and E. S. Toberer, “Complex thermoelectric materials,” *Mater. Sustain. Energy Collect. Peer-Rev. Res. Rev. Artic. Nat. Publ. Group*, pp. 101–110, 2011.

[43] J. Moore and R. Graves, “Absolute Seebeck coefficient of platinum from 80 to 340 K and the thermal and electrical conductivities of lead from 80 to 400 K,” *J. Appl. Phys.*, vol. 44, no. 3, pp. 1174–1178, 1973.

[44] H. Goldsmid and R. Douglas, “The use of semiconductors in thermoelectric refrigeration,” *Br. J. Appl. Phys.*, vol. 5, no. 11, p. 386, 1954.

[45] Z. Liu, J. Mao, J. Sui, and Z. Ren, “High thermoelectric performance of α-MgAgSb for power generation,” *Energy Environ. Sci.*, vol. 11, no. 1, pp. 23–44, 2018.

[46] T. M. Tritt and M. Subramanian, “Thermoelectric materials, phenomena, and applications: a bird’s eye view,” *MRS Bull.*, vol. 31, no. 3, pp. 188–198, 2006.

[47] T. Scheidemantel, C. Ambrosch-Draxl, T. Thonhauser, J. Badding, and J. O. Sofo, “Transport coefficients from first-principles calculations,” *Phys. Rev. B*, vol. 68, no. 12, p. 125210, 2003.

[48] J. Kangsabanik and A. Alam, “Bismuth based half-Heusler alloys with giant thermoelectric figures of merit,” *J. Mater. Chem. A*, vol. 5, no. 13, pp. 6131–6139, 2017.

[49] A. Kundu, S. Ghosh, R. Banerjee, S. Ghosh, and B. Sanyal, “New quaternary half-metallic ferromagnets with large Curie temperatures,” *Sci. Rep.*, vol. 7, no. 1, pp. 1–15, 2017.

[50] S. Chen and Z. Ren, “Recent progress of half-Heusler for moderate temperature thermoelectric applications,” *Mater. Today*, vol. 16, no. 10, pp. 387–395, 2013.

[51] Y. Pei, A. LaLonde, S. Iwanaga, and G. J. Snyder, “High thermoelectric figure of merit in heavy hole dominated PbTe,” *Energy Environ. Sci.*, vol. 4, no. 6, pp. 2085–2089, 2011.

[52] T. Graf, C. Felser, and S. S. Parkin, “Simple rules for the understanding of Heusler compounds,” *Prog. Solid State Chem.*, vol. 39, no. 1, pp. 1–50, 2011.

[53] V. Alijani, J. Winterlik, G. H. Fecher, S. S. Naghavi, and C. Felser, “Quaternary half-metallic Heusler ferromagnets for spintronics applications,” *Phys. Rev. B*, vol. 83, no. 18, p. 184428, 2011.

[54] L. Xiong, L. Yi, and G. Gao, “Search for half-metallic magnets with large half-metallic gaps in the quaternary Heusler alloys CoFeTiZ and CoFeVZ (Z= Al, Ga, Si, Ge, As, Sb),” *J. Magn. Magn. Mater.*, vol. 360, pp. 98–103, 2014.

[55] T. M. Bhat and D. C. Gupta, “Robust thermoelectric performance and high spin polarisation in CoMnTiAl and FeMnTiAl compounds,” *RSC Adv.*, vol. 6, no. 83, pp. 80302–80309, 2016.

[56] G. Xu *et al.*, “A new spin gapless semiconductors family: Quaternary Heusler compounds,” *EPL Europhys. Lett.*, vol. 102, no. 1, p. 17007, 2013.

[57] B. Hamad, “Theoretical Investigations of the Thermoelectric Properties of Fe2NbGa1−xAlx (x = 0, 0.25, 0.5) Alloys,” *J. Electron. Mater.*, vol. 46, no. 11, pp. 6595–6602, 2017, doi: 10.1007/s11664-017-5721-4.

[58] S. Wurmehl *et al.*, “Half-metallic ferromagnetism with high magnetic moment and high Curie temperature in Co 2 Fe Si,” *J. Appl. Phys.*, vol. 99, no. 8, pp. 08J103-08J103-3, 2006, doi: 10.1063/1.2167330.

[59] S. WURMEHL *et al.*, “Geometric, electronic, and magnetic structure of Co2FeSi : Curie temperature and magnetic moment measurements and calculations,” *Phys. Rev. B Condens. Matter Mater. Phys.*, vol. 72, no. 18, p. 184434.1-184434.9, 2005.

[60] J. KUBLER, “Ab initio estimates of the Curie temperature for magnetic compounds,” *J. Phys. Condens. Matter*, vol. 18, no. 43, pp. 9795–9807, 2006, doi: 10.1088/0953-8984/18/43/003.

[61] J. C. Slater, “A Simplification of the Hartree-Fock Method,” *Phys. Rev.*, vol. 81, no. 3, pp. 385–390, 1951, doi: 10.1103/PhysRev.81.385.

[62] T. Borowski and P. E. M. Siegbahn, “Chapter 4 - Density Functional Theory Studies on Non-heme Iron Enzymes,” *Iron-Contain. Enzym. Versatile Catal. Hydroxylation React. Nat.*, no. Journal Article, pp. 88–118, 2011, doi: 10.1039/9781849732987-00088.

[63] A. Sergeev, R. Jovanovic, S. Kais, and F. H. Alharbi, “Correction to kinetic energy density functional using exactly solvable model,” *Phys. Scr.*, vol. 90, no. 12, p. 125401, 2015, doi: 10.1088/0031-8949/90/12/125401.

[64] D. S. Sholl and J. A. Steckel, *Density functional theory: a practical introduction*, 1. Aufl. Hoboken, N.J: Wiley, 2009. [Online]. Available: https://go.exlibris.link/QB8cJhYz

[65] A. Y. Shul’man and D. V. Posvyanskii, “Truly self-consistent solution of Kohn-Sham equations for extended systems with inhomogeneous electron gas,” *J. Phys. Conf. Ser.*, vol. 510, no. 1, p. 12029, 2014, doi: 10.1088/1742-6596/510/1/012029.

[66] J. P. Perdew, K. Burke, and M. Ernzerhof, “Generalized Gradient Approximation Made Simple [Phys. Rev. Lett. 77, 3865 (1996)],” *Phys. Rev. Lett.*, vol. 78, no. 7, pp. 1396–1396, 1997, doi: 10.1103/PhysRevLett.78.1396.

[67] E. J. Baerends, “Perspective on ‘Self-consistent equations including exchange and correlation effects’: Kohn W, Sham LJ (1965) Phys Rev A 140:133–1138,” *Theor. Chem. Acc.*, vol. 103, no. 3, pp. 265–269, 2000, doi: 10.1007/s002140050031.

[68] Cambridge Philosophical Society, “Mathematical proceedings of the Cambridge Philosophical Society,” *Math. Proc. Camb. Philos. Soc.*, no. Journal, Electronic, [Online]. Available: https://go.exlibris.link/cbn6RjGM

[69] D. M. Ceperley and B. J. Alder, “Ground State of the Electron Gas by a Stochastic Method,” *Phys. Rev. Lett.*, vol. 45, no. 7, pp. 566–569, 1980, doi: 10.1103/PhysRevLett.45.566.

[70] G. I. Csonka *et al.*, “Assessing the performance of recent density functionals for bulk solids,” *Phys. Rev. B Condens. Matter Mater. Phys.*, vol. 79, no. 15, 2009, doi: 10.1103/PhysRevB.79.155107.

[71] H. Gudmundsdóttir, E. Ö. Jónsson, and H. Jónsson, “Calculations of Al dopant inα-quartz using a variational implementation of the Perdew–Zunger self-interaction correction,” *New J. Phys.*, vol. 17, no. 8, p. 83006, 2015, doi: 10.1088/1367-2630/17/8/083006.

[72] A. V. Arbuznikov, “Hybrid exchange correlation functionals and potentials: Concept elaboration,” *J. Struct. Chem.*, vol. 48, no. S1, pp. S1–S31, 2007, doi: 10.1007/s10947-007-0147-0.

[73] C. F. FISCHER, J. B. LAGOWSKI, and S. H. VOSKO, “Ground states of Ca- and Sc- from two theoretical points of view,” *Phys. Rev. Lett.*, vol. 59, no. 20, pp. 2263–2266, 1987.

[74] H. H. Andersen, V. V. Petrunin, P. Kristensen, and T. Andersen, “Structural properties of the negative strontium ion: Binding energy and fine-structure splitting,” *Phys. Rev. At. Mol. Opt. Phys.*, vol. 55, no. 4, pp. 3247–3249, 1997, doi: 10.1103/PhysRevA.55.3247.

[75] O. V. Gritsenko, P. R. T. Schipper, and E. J. Baerends, “Exchange and correlation energy in density functional theory: Comparison of accurate density functional theory quantities with traditional Hartree–Fock based ones and generalized gradient approximations for the molecules Li2, N2, F2,” *J. Chem. Phys.*, vol. 107, no. 13, pp. 5007–5015, 1997, doi: 10.1063/1.474864.

[76] Y. Zhao, N. E. Schultz, and D. G. Truhlar, “Exchange-correlation functional with broad accuracy for metallic and nonmetallic compounds, kinetics, and noncovalent interactions,” *J. Chem. Phys.*, vol. 123, no. 16, pp. 161103–161103, 2005, doi: 10.1063/1.2126975.

[77] A. Becke, “Density-functional exchange-energy approximation with correct asymptotic behavior,” *Phys. Rev. Gen. Phys.*, vol. 38, no. 6, pp. 3098–3100, 1988, doi: 10.1103/PhysRevA.38.3098.

[78] J. R. Hayes, “Electrical transport in the quaternary semiconductor alloy (GaIn)(AsP)/InP,” ProQuest Dissertations Publishing, 1981. [Online]. Available: https://go.exlibris.link/QnCGL6nF

[79] G. Kresse and D. Joubert, “From ultrasoft pseudopotentials to the projector augmented-wave method,” *Phys. Rev. B*, vol. 59, no. 3, p. 1758, 1999.

[80] G. Kresse and J. Hafner, “Ab initio molecular dynamics for liquid metals,” *Phys. Rev. B*, vol. 47, no. 1, p. 558, 1993.

[81] P. Blaha, K. Schwarz, P. Sorantin, and S. Trickey, “Full-potential, linearized augmented plane wave programs for crystalline systems,” *Comput. Phys. Commun.*, vol. 59, no. 2, pp. 399–415, 1990.

[82] Y. Gao and X. Gao, “The half-metallicity of LiMgPdSn-type quaternary Heusler alloys FeMnScZ (Z= Al, Ga, In): a first-principle study,” *AIP Adv.*, vol. 5, no. 5, p. 057157, 2015.

[83] R. Haleoot and B. Hamad, “Ab initio investigations of the structural, electronic, magnetic, and thermoelectric properties of CoFeCuZ (Z= Al, As, Ga, In, Pb, Sb, Si, Sn) quaternary Heusler alloys,” *J. Electron. Mater.*, vol. 48, no. 2, pp. 1164–1173, 2019.

[84] D. Hoat *et al.*, “First principles analysis of the half-metallic ferromagnetism, elastic and thermodynamic properties of equiatomic quaternary Heusler compound CoCrRhSi,” *Mater. Chem. Phys.*, vol. 257, p. 123695, 2021.

[85] R. Haleoot and B. Hamad, “Thermodynamic and thermoelectric properties of CoFeYGe (Y= Ti, Cr) quaternary Heusler alloys: first principle calculations,” *J. Phys. Condens. Matter*, vol. 32, no. 7, p. 075402, 2019.

[86] F. Kong, Y. Hu, H. Hou, Y. Liu, B. Wang, and L. Wang, “Thermoelectric and thermodynamic properties of half-Heulser alloy YPdSb from first principles calculations,” *J. Solid State Chem.*, vol. 196, pp. 511–517, 2012.

[87] M. Born and K. Huang, “Dynamical Theory of Crystal Lattices,” *Am. J. Phys.*, vol. 23, no. 7, pp. 474–474, 1955, doi: 10.1119/1.1934059.

[88] F. Kong, Y. Liu, B. Wang, Y. Wang, and L. Wang, “Lattice dynamics of PbTe polymorphs from first principles,” *Comput. Mater. Sci.*, vol. 56, pp. 18–24, 2012.

[89] Y. Zhou, X. Zhang, and M. Hu, “Quantitatively analyzing phonon spectral contribution of thermal conductivity based on nonequilibrium molecular dynamics simulations. I. From space Fourier transform,” *Phys. Rev. B*, vol. 92, no. 19, p. 195204, 2015.

[90] M. D. Santia, N. Tandon, and J. Albrecht, “Erratum:‘Lattice thermal conductivity in β-Ga2O3 from first principles’[Appl. Phys. Lett. 107, 041907 (2015)],” *Appl. Phys. Lett.*, vol. 109, no. 4, p. 049901, 2016.

[91] S. Mukhopadhyay, L. Lindsay, and D. J. Singh, “Optic phonons and anisotropic thermal conductivity in hexagonal Ge 2 Sb 2 Te 5,” *Sci. Rep.*, vol. 6, no. 1, pp. 1–8, 2016.

[92] Z. Yan and S. Kumar, “Phonon mode contributions to thermal conductivity of pristine and defective β-Ga 2 O 3,” *Phys. Chem. Chem. Phys.*, vol. 20, no. 46, pp. 29236–29242, 2018.

[93] R. Hill, “The elastic behaviour of a crystalline aggregate,” *Proc. Phys. Soc. Sect. A*, vol. 65, no. 5, p. 349, 1952.

[94] J.-S. Zhao *et al.*, “First-principles study of the structure, electronic, magnetic and elastic properties of half-Heusler compounds LiXGe (X= Ca, Sr and Ba),” *Intermetallics*, vol. 89, pp. 65–73, 2017.

[95] X. Wang, Z. Cheng, J. Wang, and G. Liu, “A full spectrum of spintronic properties demonstrated by a C1 b-type Heusler compound Mn 2 Sn subjected to strain engineering,” *J. Mater. Chem. C*, vol. 4, no. 36, pp. 8535–8544, 2016.

[96] F. Semari *et al.*, “Phase stability, mechanical, electronic and thermodynamic properties of the Ga3Sc compound: An ab-initio study,” *Inorg. Chem. Commun.*, vol. 122, p. 108304, 2020.

[97] Y. Lv, X. Zhang, and W. Jiang, “Phase stability, elastic, anisotropic properties, lattice dynamical and thermodynamic properties of B12M (M= Th, U, Np, Pu) dodecaborides,” *Ceram. Int.*, vol. 44, no. 1, pp. 128–135, 2018.

[98] X. Chen, M. Zhong, Y. Feng, Y. Zhou, H. Yuan, and H. Chen, “Structural, electronic, elastic, and thermodynamic properties of the spin-gapless semiconducting Mn2CoAl inverse Heusler alloy under pressure,” *Phys. Status Solidi B*, vol. 252, no. 12, pp. 2830–2839, 2015.

[99] R. Jain, V. K. Jain, A. R. Chandra, V. Jain, and N. Lakshmi, “Study of the Electronic Structure, Magnetic and Elastic Properties and Half-Metallic Stability on Variation of Lattice Constants for CoFeCr Z (Z= P, As, Sb) Heusler Alloys,” *J. Supercond. Nov. Magn.*, vol. 31, no. 8, pp. 2399–2409, 2018.

[100] H. Alqurashi and B. Hamad, “Magnetic structure, mechanical stability and thermoelectric properties of VTiRhZ (Z= Si, Ge, Sn) quaternary Heusler alloys: first-principles calculations,” *Appl. Phys. A*, vol. 127, no. 10, pp. 1–11, 2021.

[101] S.-C. Wu, G. H. Fecher, S. Shahab Naghavi, and C. Felser, “Elastic properties and stability of Heusler compounds: Cubic Co2 YZ compounds with L 21 structure,” *J. Appl. Phys.*, vol. 125, no. 8, p. 082523, 2019.

[102] M. Ilkhani, A. Boochani, M. Amiri, M. Asshabi, and D. P. Rai, “Mechanical stability and thermoelectric properties of the PdZrTiAl quaternary Heusler: A DFT study,” *Solid State Commun.*, vol. 308, p. 113838, 2020.

[103] Y. Li *et al.*, “First-principles study on electronic structure, magnetism and half-metallicity of the NbCoCrAl and NbRhCrAl compounds,” *Results Phys.*, vol. 7, pp. 2248–2254, 2017.

[104] M. B. Stearns, “Simple explanation of tunneling spin-polarization of Fe, Co, Ni and its alloys,” *J. Magn. Magn. Mater.*, vol. 5, no. 2, pp. 167–171, 1977.

[105] I. Galanakis, P. Dederichs, and N. Papanikolaou, “Slater-Pauling behavior and origin of the half-metallicity of the full-Heusler alloys,” *Phys. Rev. B*, vol. 66, no. 17, p. 174429, 2002.

[106] A. Mubarak, S. Saad, F. Hamioud, and M. Al-Elaimi, “Structural, thermo-elastic, electro-magnetic and thermoelectric attributes of quaternary CoNbMnX (X= Al, Si) Heusler alloys,” *Solid State Sci.*, vol. 111, p. 106397, 2021.

[107] L. Jia *et al.*, “New Quaternary Half-Metallic Materials of the Z t− 28 Rule in LiMgPdSn-Type Heusler Alloys,” *J. Supercond. Nov. Magn.*, vol. 31, no. 4, pp. 1067–1072, 2018.

[108] A. Candan, G. Uğur, Z. Charifi, H. Baaziz, and M. Ellialtıoğlu, “Electronic structure and vibrational properties in cobalt-based full-Heusler compounds: A first principle study of Co2MnX (X= Si, Ge, Al, Ga),” *J. Alloys Compd.*, vol. 560, pp. 215–222, 2013.

[109] M. Elahmar *et al.*, “Structural, mechanical, electronic and magnetic properties of a new series of quaternary Heusler alloys CoFeMnZ (Z= Si, As, Sb): a first-principle study,” *J. Magn. Magn. Mater.*, vol. 393, pp. 165–174, 2015.

[110] M. Geilhufe *et al.*, “Effect of hydrostatic pressure and uniaxial strain on the electronic structure of Pb 1− x Sn x Te,” *Phys. Rev. B*, vol. 92, no. 23, p. 235203, 2015.

[111] L. Xi *et al.*, “Chemical bonding, conductive network, and thermoelectric performance of the ternary semiconductors Cu 2 Sn X 3 (X= Se, S) from first principles,” *Phys. Rev. B*, vol. 86, no. 15, p. 155201, 2012.

[112] D. Parker and D. J. Singh, “High-temperature thermoelectric performance of heavily doped PbSe,” *Phys. Rev. B*, vol. 82, no. 3, p. 035204, 2010.

[113] H. Wang, W. Chu, and H. Jin, “Theoretical study on thermoelectric properties of Mg2Si and comparison to experiments,” *Comput. Mater. Sci.*, vol. 60, pp. 224–230, 2012.

[114] T. Thonhauser, T. Scheidemantel, J. Sofo, J. Badding, and G. Mahan, “Thermoelectric properties of Sb 2 Te 3 under pressure and uniaxial stress,” *Phys. Rev. B*, vol. 68, no. 8, p. 085201, 2003.

[115] S. A. Khandy and J.-D. Chai, “Thermoelectric properties, phonon, and mechanical stability of new half-metallic quaternary Heusler alloys: FeRhCrZ (Z= Si and Ge),” *J. Appl. Phys.*, vol. 127, no. 16, p. 165102, 2020.

[116] G. Mahan and J. Sofo, “The best thermoelectric,” *Proc. Natl. Acad. Sci.*, vol. 93, no. 15, pp. 7436–7439, 1996.

[117] J. O. Sofo and G. Mahan, “Optimum band gap of a thermoelectric material,” *Phys. Rev. B*, vol. 49, no. 7, p. 4565, 1994.

[118] Z. M. Gibbs, H.-S. Kim, H. Wang, and G. J. Snyder, “Band gap estimation from temperature dependent Seebeck measurement—Deviations from the 2e| S| maxTmax relation,” *Appl. Phys. Lett.*, vol. 106, no. 2, p. 022112, 2015.

[119] E. H. Hasdeo, L. P. Krisna, M. Y. Hanna, B. E. Gunara, N. T. Hung, and A. R. Nugraha, “Optimal band gap for improved thermoelectric performance of two-dimensional Dirac materials,” *J. Appl. Phys.*, vol. 126, no. 3, p. 035109, 2019.

[120] T. Lin, Q. Gao, G. Liu, X. Dai, X. Zhang, and H. Zhang, “Dynamical stability, electronic and thermoelectric properties of quaternary ZnFeTiSi Heusler compound,” *Curr. Appl. Phys.*, vol. 19, no. 6, pp. 721–727, 2019.

[121] S. Singh and D. C. Gupta, “Lanthanum based quaternary Heusler alloys LaCoCrX (X= Al, Ga): Hunt for half-metallicity and high thermoelectric efficiency,” *Results Phys.*, vol. 13, p. 102300, 2019.

[122] A. Hong *et al.*, “Full-scale computation for all the thermoelectric property parameters of half-Heusler compounds,” *Sci. Rep.*, vol. 6, no. 1, pp. 1–12, 2016.

[123] H. Ma, C.-L. Yang, M.-S. Wang, X.-G. Ma, and Y.-G. Yi, “Effect of M elements (M= Ti, Zr, and Hf) on thermoelectric performance of the half-Heusler compounds MCoBi,” *J. Phys. Appl. Phys.*, vol. 52, no. 25, p. 255501, 2019.

[124] R. Haleoot and B. Hamad, “Thermoelectric properties of doped β-InSe by Bi: first principle calculations,” *Phys. B Condens. Matter*, vol. 587, p. 412105, 2020.

[125] G. A. Slack, “Nonmetallic crystals with high thermal conductivity,” *J. Phys. Chem. Solids*, vol. 34, no. 2, pp. 321–335, 1973.

[126] C. Li and Z. Wang, “Computational modelling and ab initio calculations in MAX phases–I,” *Adv. Sci. Technol. Mn 1AXn Phases*, pp. 197–222, 2012.

Appendix A: List of Equations